Seasonal and inter-annual variability of carbon fluxes in southern Africa seen by GOSAT

Eva-Marie Metz[1], Sanam Noreen Vardag[1,2], Sourish Basu[3,4], Martin Jung[5], André Butz[1,2,6]

[1]Institute of Environmental Physics, Heidelberg University, Heidelberg, 69120, Germany
5 [2]Heidelberg Center for the Environment (HCE), Heidelberg University, Heidelberg, 69120, Germany.
[3]Goddard Space Flight Center, NASA, Greenbelt, MD 20771, USA
[4]Earth System Science Interdisciplinary Center, University of Maryland, College Park, MD 20740, USA
[5]Max Planck Institute for Biogeochemistry, Jena, 07745, Germany
[6]Interdisciplinary Center for Scientific Computing (IWR), Heidelberg University, Heidelberg, 69120, Germany

10 *Correspondence to*: Eva-Marie Metz (eva-marie.metz@iup.uni-heidelberg.de)

Abstract. The inter-annual variability of the global carbon sink is heavily influenced by semi-arid regions. Southern hemispheric Africa has large semi-arid and arid regions. However, there is only a sparse coverage of in situ CO_2 measurements on the southern hemisphere. This leads to uncertainties in measurement-based carbon flux estimates for these regions. Also, dynamic global vegetation models (DGVMs) show large inconsistencies in semi-arid regions. Satellite CO_2

15 measurements offer a spatially extensive and independent source of information about the southern African carbon cycle.

We examine Greenhouse Gases Observing Satellite (GOSAT) CO_2 concentration measurements from 2009 to 2018 in southern Africa. We infer CO_2 land-atmosphere fluxes which are consistent with the GOSAT measurements using the atmospheric inversion system TM5-4DVar. We find systematic differences between these satellite-based carbon fluxes and atmospheric inversions based on in situ measurements pointing towards a limited measurement information content in the

20 latter. We use the GOSAT based fluxes and additionally Solar Induced Fluorescence (SIF), a proxy for photosynthesis, as atmospheric constraints to select DGVMs of the TRENDYv9 ensemble which show compatible fluxes. The selected DGVMs allow for studying the vegetation processes driving the southern African carbon cycle. We show that the variability of photosynthetic uptake mainly drives the inter-annual variability of the southern African carbon fluxes. The seasonal cycle, however, is substantially influenced by enhanced soil respiration due to soil rewetting at the beginning of the rainy season.

25 The latter result emphasizes the importance of correctly representing the response of semi-arid ecosystems to soil rewetting in DGVMs.

1 Introduction

The terrestrial carbon sink currently takes up nearly one third of human made greenhouse gases and thereby slows down climate change (Friedlingstein et al., 2023). The amount of CO_2 taken up by global ecosystems varies substantially from year

30 to year. This inter-annual variability (IAV) reflects the response of ecosystem carbon uptake to varying climate conditions such as temperature or precipitation fluctuations (Zeng et al., 2005; Zhang et al., 2018; Piao et al., 2020). Current vegetation

models struggle in accurately reproducing IAV of the terrestrial carbon sink and an imbalance exists between the modelled and measured total global sink estimates (Friedlingstein et al., 2023). The imbalance is even stronger when examining carbon fluxes on smaller spatial scales (Bastos et al., 2020) and implies that there is still an insufficient understanding of the
35 terrestrial processes driving land carbon exchange. A better understanding is needed to improve climate models and climate change predictions (Steiner et al., 2020).

Semi-arid regions contribute substantially to the IAV of the global terrestrial carbon sink. In these regions, precipitation and temperature fluctuations heavily impact the IAV of carbon fluxes (Poulter et al., 2014; Ahlström et al., 2015). Africa has large areas of semi-arid and arid ecosystems (Williams et al., 2007) and contributes substantially to the global IAV
40 (Williams et al., 2007; Valentini et al., 2014; Pan et al., 2020). However, in situ CO_2 measurements in Africa are very sparse leading to large uncertainties in carbon flux estimates from atmospheric inversions and machine learning approaches (Valentini et al., 2014; Ernst et al., 2024). Dynamic Global Vegetation Models (DGVMs), also, show large inconsistencies amongst each other and tend to underestimate the inter-annual CO_2 flux variability in semi-arid regions (MacBean et al., 2021).

45 Satellite CO_2 concentration measurements, for example from the Greenhouse Gases Observing Satellite (GOSAT) measuring CO_2 concentrations since 2009 or the Orbiting Carbon Observatory 2 (OCO-2) launched in 2014, have much denser coverage compared to in situ measurements. Previous studies found systematic differences between satellite- and in situ measurement-based CO_2 concentrations and fluxes in southern Africa (Mengistu and Mengistu Tsidu, 2020; Taylor et al., 2022; Byrne et al., 2023). Byrne et al. (2023) attribute these differences mainly to the sparse coverage of in situ CO_2
50 measurements. The studies emphasize the potential of satellite-based atmospheric inversions to provide additional information and therefore more robust estimates of the carbon fluxes in southern hemispheric Africa, which then enable research about processes driving the CO_2 exchange. Metz et al. (2023) demonstrate the potential of combining satellite-based CO_2 flux estimates with DGVMs in Australia to decipher soil respiration processes driving the Australian terrestrial CO_2 exchange on continental scale.

55 Here, we investigate the decadal dataset of GOSAT CO_2 concentrations over southern hemispheric Africa from 2009 to 2018. We run a global inversion with GOSAT and in situ measurements to infer GOSAT satellite-based CO_2 exchange fluxes between land and atmosphere and compare the fluxes to flux estimates based on in situ measurements alone, to machine learning approaches, and to the TRENDYv9 ensemble of DGVMs. By selecting a subset of DGVMs which match the satellite-based carbon fluxes, we analyse the underlying processes driving the IAV and seasonal variability of the
60 southern African carbon cycle.

2 Data and Methods

2.1 Study region

Our study region spans southern hemispheric Africa southwards of 10° S including Madagascar (see Fig. 1). This region agrees with the region selection in Mengistu and Mengistu Tsidu (2020) taking into account the different climatic conditions

65 in the African continent. Northwards of the study region, Africa is influenced by the low pressure system of the inter tropical convergence zone leading to a tropical wet regime. In the southern Africa, high pressure cells lead to dry conditions and cause the existence of the Kalahari Desert (Mengistu and Mengistu Tsidu, 2020). Even though total annual precipitation is decreasing southwards, the whole region experiences distinct wet and dry seasons and is influenced strongly by IAV of precipitation (Fan et al., 2015; Valentinti et al., 2015). The study region is mainly covered by (woody) savannas, grassland,

70 and shrubland (see Fig. 1).
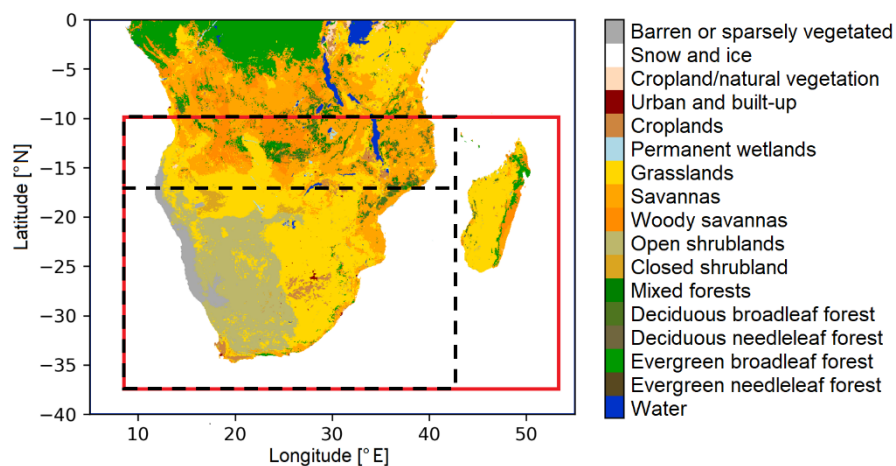
Figure 1: Study region southern Africa. The land cover in the study region is given based on MODIS (MCD12C1) data (Friedl and Sulla-Menashe, 2022). Additionally, the main region used for the analyses is depicted as a red box. The black dashed boxes show the subdivision into a northern and southern region.

75 The vegetation is mostly water limited in its growth (Williams et al., 2008) and exposed to large seasonal fires. The fire season starts in May in the western part of Africa and spreads eastwards to reach southern Africa in September (Edwards et al., 2006). Fires on the whole African continent are the largest contributor to and account for more than half of the global fire carbon emissions (van Marle et al., 2017; Shi et al., 2015; Valentini et al., 2014). They reduce the African carbon sink significantly (Lasslop et al., 2020). We subdivide the study region in a northern, savanna dominated region and a southern

80 grass- and shrubland region separated at 17°S, excluding Madagascar.

2.2 Total column CO₂ measurements

For our analyses we use column-average dry-air mole fractions of CO_2 (XCO₂, in the following referred to as CO_2 concentrations) measured by the Greenhouse Gases Observing Satellite (GOSAT). GOSAT was launched in 2009 and has a sub-satellite field of view of 10.5 km radius with a sparse sampling grid. We use GOSAT CO_2 concentration data generated

85 by applying the RemoTeC radiative transfer and retrieval algorithm version 2.4.0 (Butz, 2022) as used in Metz et al. (2023). The retrieval version is based on the preceding RemoTeCv2.3.8 as used in Detmers et al. (2015) and covers the period 04/2009–06/2019. Moreover, GOSAT CO_2 concentration data generated by the NASA Atmospheric CO_2 Observation from Space (ACOS) algorithm version 9 (Lite), available for the period 04/2009-07/2020, is used. In the following the datasets are called GOSAT/RemoTeC and GOSAT/ACOS (see Table A1 for more information about the datasets and nomenclature used

90 in this study).

For validation purposes, XCO₂ data measured by the Orbiting Carbon Observatory 2 (OCO-2) satellite is used (OCO-2/OCO-3 Science Team, 2020; Eldering et al., 2017). OCO-2 was launched in 2014 and has a sub-satellite field of view of 1.3 km x 2.3 km. Furthermore, Collaborative Carbon Column Observing Network (COCCON) XCO₂ data of the Gobabeb station (Namibia, Frey et al., 2021; Dubravica, 2021) is taken for comparison. COCCON stations measure XCO₂ using a

95 sun-viewing ground-based Fourier transform infrared spectrometer (Frey et al., 2019).

For examining the seasonal variability of CO_2 concentrations in the study region, the global background trend is subtracted from the total CO_2 measurements to obtain detrended CO_2 concentrations. For this, we assume a yearly linear increase of global atmospheric CO_2 and use the annual mean CO_2 growth rate (GR) published by the National Oceanic and Atmospheric Administration (NOAA). The growth rates are based on globally averaged CO_2 concentration measurements of marine

100 surface sites (NOAA, 2024). The following equation describes the used background trend:

$$BG_{y,m} = BG_0 + \sum_{i=2009}^{y-1}(GR_i) + \frac{m}{12}GR_y \, . \tag{1}$$

Thereby, the increase of the CO_2 concentrations in the previous years from 2009 onwards is described by the second part in the equation. The increase within the previous months in the respective year is given by the third part. Both are added to an overall offset BG_0 in 2009. This offset is estimated so that the mean of the detrended CO_2 concentrations over the whole time

105 period is zero.

2.3 Fluxes

2.3.1 Top-down

Carbon fluxes can be obtained by assimilating measured CO_2 atmospheric concentrations in an atmospheric inversion.

110 Atmospheric inversions typically build on Bayesian optimization i.e. they optimize forward transported CO_2 emissions such that these agree best with the observations within measurement and model uncertainties, while at the same time not deviating

from the prior within given prior uncertainties. For our study, we use three in situ CO_2 measurement based atmospheric inversions: the TM5 four-dimensional variational inversion system (TM5-4DVar, (Basu et al., 2013)), NOAA's modelling and assimilation system CarbonTracker (CT2022, (Peters et al., 2007; Jacobson et al., 2023)), and Copernicus Atmosphere

115   Monitoring Service (CAMS, (Chevallier et al., 2005; Chevallier et al., 2010; Chevallier et al., 2019)). The models estimate global CO_2 fluxes based on a set of in situ CO_2 measurements from global monitoring networks (Masarie et al., 2014). Thereby, the models use different prior datasets. For example, for the biogenic CO_2 fluxes, TM5-4DVar and CarbonTracker build on different implementations of the Carnegie-Ames-Stanford Approach (Randerson et al., 1996) as further described in Metz et al. (2023), Weir et al. (2021), and Jacobson et al. (2023), while CAMS uses biogenic fluxes of the ORCHIDEE

120   model (Chevallier et al., 2019). Furthermore, the models use different transport models. While TM5-4DVar and CarbonTracker use the transport model TM5, CAMS uses the LMDZ global atmospheric transport model. All three models use ECMWF ERA5 data as meteorological drivers. The output resolution is monthly 3°x2° for TM5-4DVar and CarbonTracker2022 and monthly 3.7°×1.81° for CAMS (see Table A1 for more details). The ensemble of the three models is referred to as in-situ-only inversions in the following, TM5-4DVar based on in situ measurements is called TM5-4DVar/IS.

125   In addition to in situ measurements, satellite CO_2 concentration measurements can be fed into atmospheric inversions. To this end, we use the model TM5-4DVar and assimilate GOSAT CO_2 concentration measurements together with the in situ measurements. Depending on the specific GOSAT dataset used, we refer to these fluxes in the following as TM5-4DVar/RemoTeC+IS, TM5-4DVar/ACOS+IS, or when using the mean of both TM5-4DVar/GOSAT+IS. More details about the TM5-4DVar settings can be found in Metz et al. (2023). For comparison we also draw on data of the OCO-2 Model

130   Intercomparison Project (MIP) (Byrne et al., 2023) for the years 2015 to 2018. Within MIP, atmospheric inversions estimate carbon fluxes assimilating OCO-2 satellite CO_2 data together with in situ data. Thereby, all MIP inversion models use the same fossil fuel emission dataset but differ in the chosen datasets for all other prior fluxes (Byrne et al., 2023). We specifically make use of the LNLGIS (OCO-2 satellite data with in situ data) and the IS (in situ data only) experiment in the following referred to as MIP/OCO-2+IS and MIP/IS, respectively. Like Byrne et al. (2023), we exclude the MIP model LoFI

135   as it uses a non-traditional inversion scheme differing from the MIP protocol. MIP/OCO+IS and MIP/IS provide fluxes with monthly 1°x1° resolution.

All inversions optimize for biogenic and oceanic fluxes but impose anthropogenic fossil fuel emissions and fire emissions. The sum of (imposed) fire and biogenic fluxes yields our net biome productivity (NBP) estimates. In this study, positive fluxes denote a release of CO_2 from land into the atmosphere. All fluxes are regridded to monthly 1°x1° fluxes before

140   performing the region selection.

By transporting the posterior fluxes after the optimization, atmospheric inversions can model posterior concentration fields, which can be interpolated to the time and location of the satellite measurements for comparison. This so-called cosampling is used to eliminate sampling errors when comparing modelled concentrations to satellite measurements. We use the modelled and co-sampled posterior concentrations of the in-situ-only inversions introduced at the beginning of this section.

2.3.2 Bottom-up

We compare the top-down CO_2 fluxes to bottom-up flux datasets from DGVMs as collected by the TRENDY Intercomparison v9 project. These TRENDY models give vegetation CO_2 fluxes simulated using a harmonized set of meteorological input data (Friedlingstein et al., 2020). We use the NBP, gross primary productivity (GPP), autotrophic respiration (RA), and heterotrophic respiration (RH) of 18 DGVMs (see Table A1). We thereby use the following definition:

$$NBP = NEE + fire + fluc = TER - GPP + fire + fluc = RH - NPP + fire + fluc \,, \tag{2}$$

with the total ecosystem respiration (TER) calculated as sum of RA and RH, the fire emissions (fire), the land-use change fluxes (fluc), and the net primary productivity (NPP) calculated as GPP – RA. Most of the TRENDY models provide NBP fluxes directly. In the case of the models CABLE-POP and DLEM, NBP is calculated as RH-NPP, as both models do not provide fire and land-use change fluxes. The spatial resolutions of the model output differ (see Table A1). Therefore, we aggregate fluxes on a monthly 1°x1° grid before applying the region selection.

Additionally, we use the FLUXCOM net ecosystem exchange (NEE) product as described in Jung et al. (2020). FLUXCOM uses machine learning models and meteorological data to upscale eddy covariance tower CO_2 flux measurements to global scale (Tramontana et al., 2016; Jung et al., 2020). To obtain an NBP estimate, we combine the NEE fluxes with fire CO_2 emissions provided by the Global Fire Emission Database (GFED, van der Werf et al., 2017). FLUXCOM and GFED are provided as 0.08°x0.08° 8-day fluxes and 0.25°x0.25° daily fluxes, respectively, and are aggregated on a monthly 1°x1° grid before applying the region selection.

2.4 Other datasets

To investigate the climatic conditions influencing the carbon fluxes, we use temperature, upper layer soil moisture, and precipitation datasets of the European Centre for Medium Range Weather Forecasts (ECMWF) ERA5-land data product (Muñoz Sabater et al., 2019; Muñoz Sabater et al., 2021) with monthly resolution on a 0.25°x0.25° spatial grid. ERA5 datasets are aggregated on a 1°x1° grid before performing the region selection. Furthermore, we use Solar Induced fluorescence (SIF) measurements by the GOME-2 satellite from 2009 to 01/2018 (Joiner et al., 2023). SIF is considered proportional to GPP and can therefore be used as a proxy for CO_2 uptake by photosynthesis (Li et al., 2018).

3 Results

3.1 Monthly CO_2 concentrations by atmospheric inversions

To access the seasonal and inter-annual dynamics in southern Africa, we detrend the monthly mean CO_2 concentrations following Eq. (1) (see Methods Sec. 2.2). The remaining CO_2 enhancements for the study region are shown in Fig. 2. The GOSAT measured CO_2 enhancements reveal a clear seasonal cycle with minimum concentration in the first and maximum

concentrations in the second half of the year. This general seasonal timing is confirmed by the posterior concentrations of the in-situ-only inversions. However, yearly reoccurring differences between GOSAT and the in-situ-only based CO_2 enhancements from September to November are clearly visible. The difference pattern has already been described by Mengistu and Mengistu Tsidu (2020) and has been shown by Taylor et al. (2022). Furthermore, especially in the second half of the year, different in-situ-only inversions are not consistent as indicated by the large shading in Fig. 2 Panel (a) (see also the individual models in Fig. A1). Reasons for these discrepancies will be further analysed in Sect. 3.3.
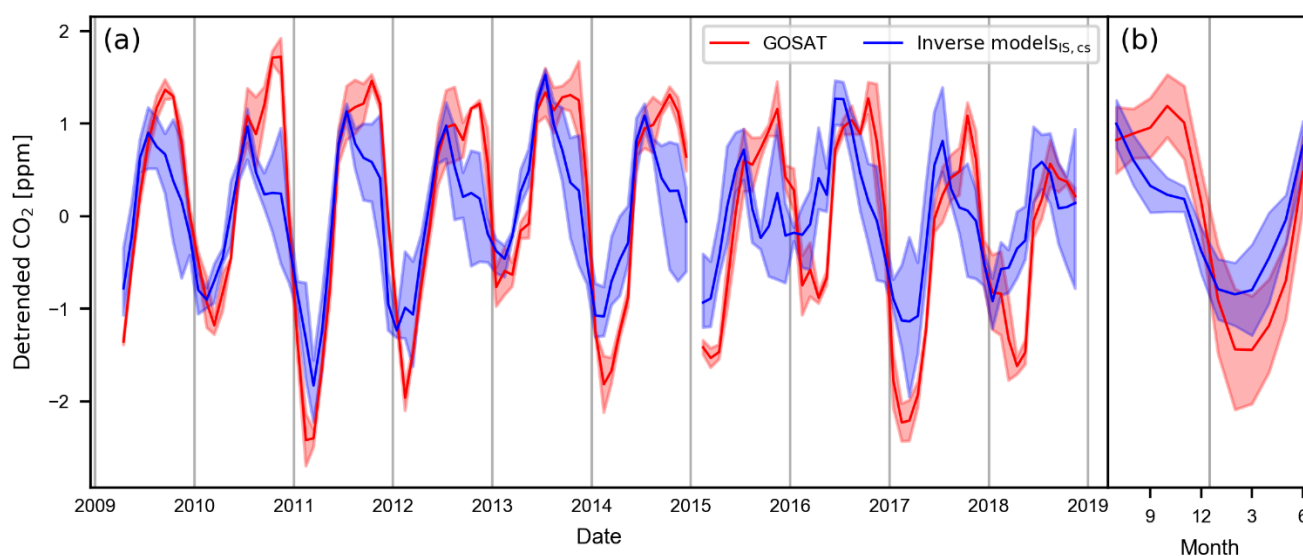
Figure 2: Monthly southern African detrended CO_2 concentrations. GOSAT measured and detrended CO_2 concentrations are depicted in red. Modelled posterior CO_2 concentrations of three in-situ-only inversions are cosampled on GOSAT and depicted as mean in blue. Panel (a) shows the monthly mean CO_2 concentrations. The shading indicates the range among the individual ensemble members (GOSAT/ACOS+IS and GOSAT/RemoTeC+IS in red, CT2022, CAMS, and TM5-4DVar/IS in blue). Panel (b) shows the mean seasonal cycle 2009–2018 with the standard deviation over the years as shading.

For comparison, we additionally use the OCO-2 satellite, which was launched in 2014, and one year of COCCON CO_2 column measurements in Namibia. Both datasets show a similar seasonal cycle as seen by GOSAT, i. e. they show concentration maxima later in the year than the in-situ-only inversions (see Fig. A1 and Fig. A2). No other total column measurement sites (e. g. of the COCCON network or Total Carbon Column Observing Network (TCCON, Wunch et al., 2011)) with coinciding consecutive measurements for more than one year exist in southern hemisphere continental Africa, limiting the validation possibilities of satellite total column measurements in this region.

3.2 Southern African top-down and bottom-up CO₂ fluxes
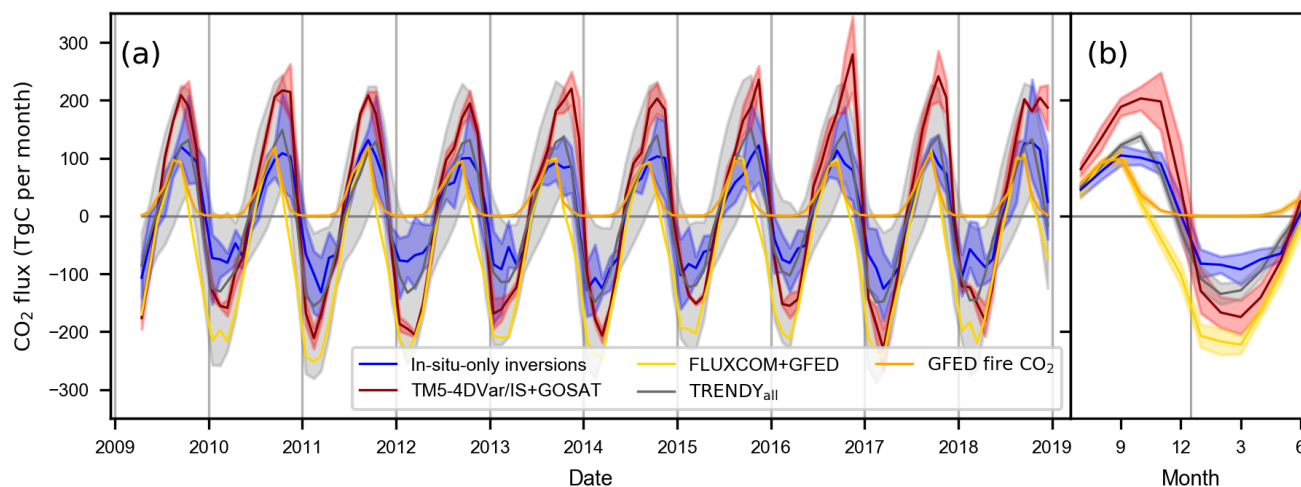
Figure 3: Top-down and bottom-up southern African net CO₂ fluxes. Panel (a) shows the mean monthly net CO₂ fluxes for the southern African region, Panel (b) shows the mean seasonal cycle of the fluxes over the 2009 to 2018 period. The TM5-4DVar/GOSAT+IS fluxes are given in red, in-situ-only inversion fluxes are shown in blue. The mean over all TRENDY models is given in grey. GFED fire emissions are shown in orange and in combination with FLUXCOM NEE in yellow. The shading indicates the range over the GOSAT based fluxes (TM5-4DVar/ACOS+IS and TM5-4DVar/RemoTeC+IS) and the in-situ-only inversion fluxes (CT2022, CAMS, and TM5-4DVar/IS) and the standard deviation over the TRENDY ensemble in Panel (a). In Panel (b) shading indicates the standard deviation over the years. Positive fluxes indicate emissions into the atmosphere. Negative fluxes correspond to an uptake of CO₂ into the land surface.

Assimilating the GOSAT CO₂ concentration measurements in TM5-4DVar, we obtain GOSAT based top-down fluxes in monthly resolution for the study region (see methods Sec. 2.3.1). As for the concentrations, a clear seasonal cycle is visible (Fig. 3). From January to May CO₂ is taken up by the land surface with a maximum uptake around March. From June to December, CO₂ is released into the atmosphere and reaches a maximum flux in September to November. A similar timing of the seasonal cycle is also captured by the in-situ-only inversion fluxes (CAMS, CT2022, and TM5-4DVar/IS). However, the in-situ-only inversions' seasonal amplitude is smaller than for TM5-4DVar/GOSAT+IS.

To analyse the found differences between TM5-4DVar/GOSAT+IS and the in-situ-only atmospheric inversions, we evaluate the information content provided by the measurements about the southern African carbon fluxes. To this end, we compare the TM5-4DVar fluxes (TM5-4DVar/IS and TM5-4DVar/GOSAT+IS) to the prior fluxes of the inversion model. From Fig. 4 it becomes clear that the in-situ-only fluxes (TM5-4DVar/IS) mainly follow the dynamics of the prior fluxes, whereas the GOSAT based fluxes deviate significantly from the prior. This is expected as the sparse coverage of in situ measurements in Africa and the southern hemisphere in general provides only little information about the African carbon fluxes. In contrast, satellites provide nearly global coverage of CO₂ measurements. Using these measurements in TM5-4DVar, new information about the southern African carbon fluxes can be obtained and lead to a deviation of TM5-4DVar/GOSAT+IS from the prior. This finding also explains the differences among the three in-situ-only inversions (see

shaded range of the in-situ-only inversions in Fig. 3). The inversions assume different prior fluxes, which they follow closely, as the information of the in situ data does not substantially inform the inversion.
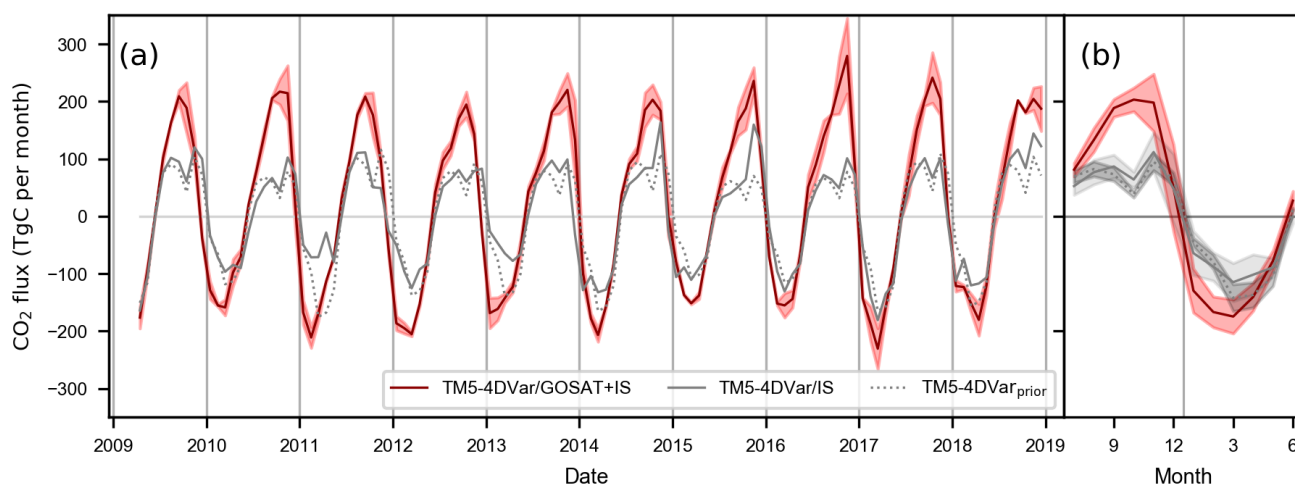
Figure 4: Top-down southern African net CO₂ fluxes from TM5-4DVar. In Panel (a), mean monthly net CO₂ fluxes for the southern African region from the TM5-4DVar prior (grey dotted), the in-situ-only inversion TM5-4DVar/IS (grey solid) and the TM5-4DVar/GOSAT+IS inversion (red) are given. Red shading indicates the range of the TM5-4DVar/ACOS+IS and TM5-4DVar/RemoTeC+IS inversions. Panel (b) shows the mean seasonal cycle 2009–2018 with the standard deviation over the years as shading.

When assimilating OCO-2 satellite measurements instead of GOSAT measurements, the MIP/OCO-2+IS ensemble mean also shows a larger amplitude of the southern African carbon fluxes compared to in-situ-only inversions and MIP/IS (Fig. 5). However, the spread among the MIP/OCO-2+IS models is large, especially during the maximum emissions from September to November. Some models show lower emissions similar to the in-situ-only inversions, whereas others agree with TM5-4DVar/GOSAT+IS. By analysing the performance of the individual models in these three months, we find that three MIP/OCO-2+IS models reproduce the OCO-2 measurements the best (see Fig. A3) indicating that the OCO-2 measurements were given a considerable weight in the inversion and thus, that the optimized fluxes were informed by measurements. At the same time, these three inversion models (Baker, CAMS, and TM5-4DVar/OCO+IS) show the largest CO₂ emissions and agree best with TM5-4DVar/GOSAT+IS (see Fig.5 and Fig. A3). Concluding, we find that satellite-based inversions, which are actually compatible to the satellite measurements, show larger carbon fluxes in southern Africa than in-situ-only inversions, which suffer from the limited information provided by the sparse in situ measurements for southern Africa.
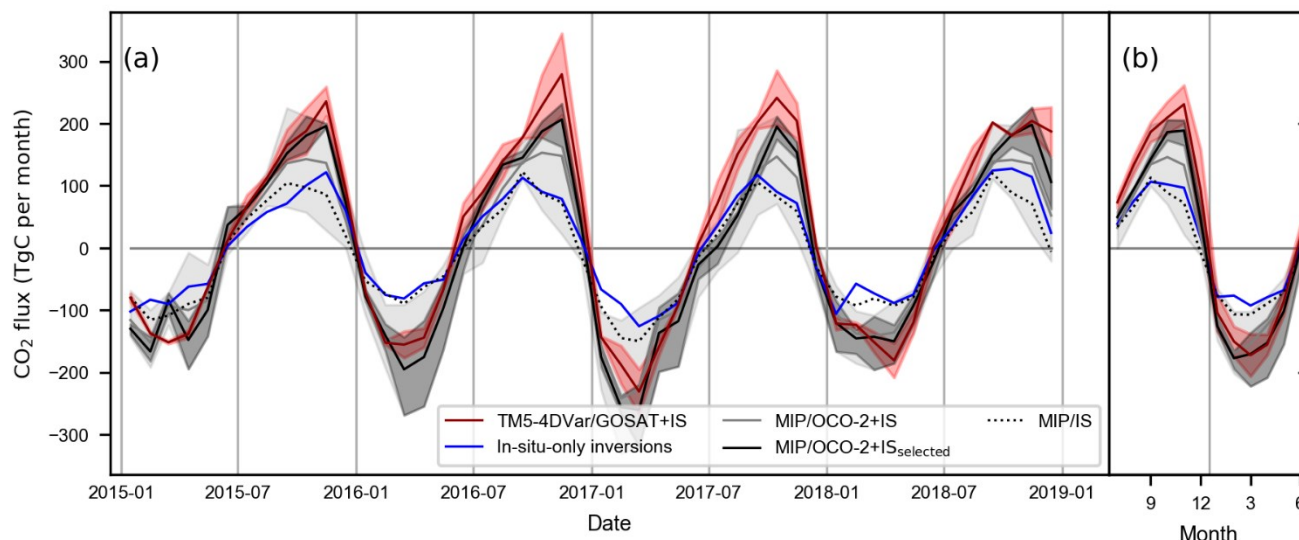
Figure 5: Top-down southern African net CO₂ fluxes from MIP. In Panel (a) mean monthly net CO₂ fluxes for the study region are given by TM5-4DVar/GOSAT+IS in red, the MIP/OCO-2+IS ensemble mean in grey, and the mean over three selected MIP models (CAMS, TM5-4DVar, and Baker) in black. In-situ-only inversion fluxes are given in blue as mean of CAMS, CT2022 and TM5-4Dvar/IS and in black dotted from the MIP/IS ensemble. The shading indicates the range over the GOSAT fluxes (TM5-4DVar/ACOS+IS and TM5-4DVar/RemoTeC+IS), the MIP ensemble, and the three selected MIP models. Panel (b) gives the mean seasonal cycle from 2015 to 2018 with shading indicating the range over the MIP ensembles' models and the standard deviation of the TM5-4DVar/GOSAT+IS over the years.

Next to the in-situ-only inversion fluxes, we compare the TM5-4DVar/GOSAT+IS fluxes to FLUXCOM CO₂ fluxes. As FLUXCOM only provides NEE fluxes, we add GFED fire CO₂ emissions to obtain a NBP estimate. In Fig. 3, FLUXCOM+GFED only reaches positive monthly fluxes from June to September due to fire emissions occurring during that time. From October to May it shows a net CO₂ uptake. While the timing of the maximum sink agrees well between FLUXCOM+GFED and the inversion fluxes, FLUXCOM+GFED shows a smaller amplitude and an earlier drop in emissions compared to TM5-4DVar/GOSAT+IS and in-situ-only inversion fluxes. The tendency of FLUXCOM to report a stronger carbon sink on the southern hemisphere compared to other datasets is described in Jung et al. (2020). It is expected that the sparsity of eddy-covariance towers in Africa or in similar ecosystems hampers the machine-learning based approach of FLUXCOM for estimating CO₂ fluxes in the study area. Jung et al. (2020) describe larger uncertainties due to representation errors in semi-arid regions.

Finally, we compare the inversion results to the ensemble of processed based vegetation models of the TRENDYv9 project. The mean of the DGVM ensemble in Panel (a) of Fig. 3 shows a smaller amplitude than the GOSAT fluxes and compares with the in-situ-only inversion fluxes. However, as indicated by the large standard deviation, the models deviate substantially from each other. Foster et al. (2024) and Metz et al. (2023) observed a similar large spread among DGVMs for the North American Temperate region and Australia, respectively. Both studies highlight the importance of performing a sub-selection of DGVMs agreeing well with atmospheric CO₂ measurements.

3.3 GOSAT and SIF atmospheric constraints on TRENDY models

260   Given the large spread of the TRENDY models, we select DGVMs according to their agreement with the GOSAT based CO_2 fluxes and SIF. Thereby, we compare the monthly mean DGVM and TM5-4DVar/GOSAT+IS NBP and NEE fluxes based on the RMSE of the monthly fluxes and the agreement in the seasonality. For the well matching DGVMs, we additionally compare the GPP normalized mean seasonal cycle to the GOME SIF normalized mean seasonal cycle. Only models with a timing of the minimum and maximum GPP agreeing within +-1 month with the normalized SIF seasonal cycle

265   are selected (see Fig. 6). This ensures the correct seasonal timing of the modelled GPP fluxes. Based on these criteria, we select the models ORCHIDEE (RMSE NBP: 60.2 TgC/month, RMSE NEE: 68,2 TgC/month), ORCHIDEEv3 (RMSE NBP 70.2 TgC/month, RMSE NEE: 56.2 TgC/month) and CABLE-POP (RMSE NBP: 78.2 TgC/month, RMSE NEE: 63.6 TgC/month). The model OCN, which performs well for NBP/NEE, shows larger deviations in the SIF/GPP comparison (see Fig. 6) and is therefore not included in the TRENDY selection.
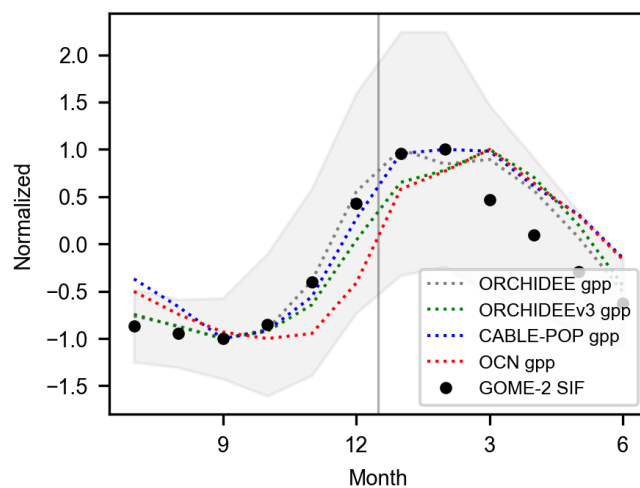
Figure 6: Seasonal cycle of SIF and selected TRENDY models. The normalized mean seasonal cycle of GOME-2 SIF (2009–01/2018), the three selected DGVMs (ORCHIDEE, ORCHIDEEv3, CABLE-POP) GPP, and OCN GPP (2009–2018) are shown in solid black and coloured dotted, respectively. The spatial standard deviation over monthly GOME-2 SIF aggregated on a 1°x1° is given as shading.

    The NBP mean over these three models is given in Panels (a) and (b) of Fig. 7. The models reproduce the timing and

275   strength of the TM5-4DVar/GOSAT+IS NBP fluxes. Only at the beginning of the emission period around July to September, the TRENDY selection fluxes are lower. Furthermore, the selection shows a significantly smaller sink in 2012 and smaller source in 2016. Note that ORCHIDEE is part of the TRENDY selection and is also used by the in-situ-only inversion CAMS as prior flux assumption. This explains why CAMS best matches TM5-4DVar/GOSAT+IS CO_2 fluxes and GOSAT CO_2 concentrations in Fig. 3 and Fig. 2, respectively.

280   Fire emissions contribute substantially to the seasonality of the southern African carbon fluxes. They largely explain the beginning of the emission period from July to September (see Fig. 3). Different fire emission data products differ

significantly and suggest large uncertainties on the magnitude of the actual fire emissions in our study region (see Fig. A4). GFED, which we use for our analyses, shows the largest fire emissions but could even underestimate the actual emissions as suggested by current literature for southern hemispheric Africa (Ramo et al., 2021).

285   To exclude the influence of fire emission in the comparison, we analyse the monthly NEE fluxes of the TRENDY selection compared to the TM5-4DVar/GOSAT+IS NBP fluxes with GFED fire emissions subtracted. The subtraction of the fire emissions leads to a better agreement between both datasets, especially at the beginning of the emission period suggesting that fire fluxes in the DGVMs do not agree to the GFED fire fluxes (see Fig. 7 Panels (c) and (d)). This goes along with large uncertainties in DGVM fire fluxes being reported previously (Bastos et al., 2020).
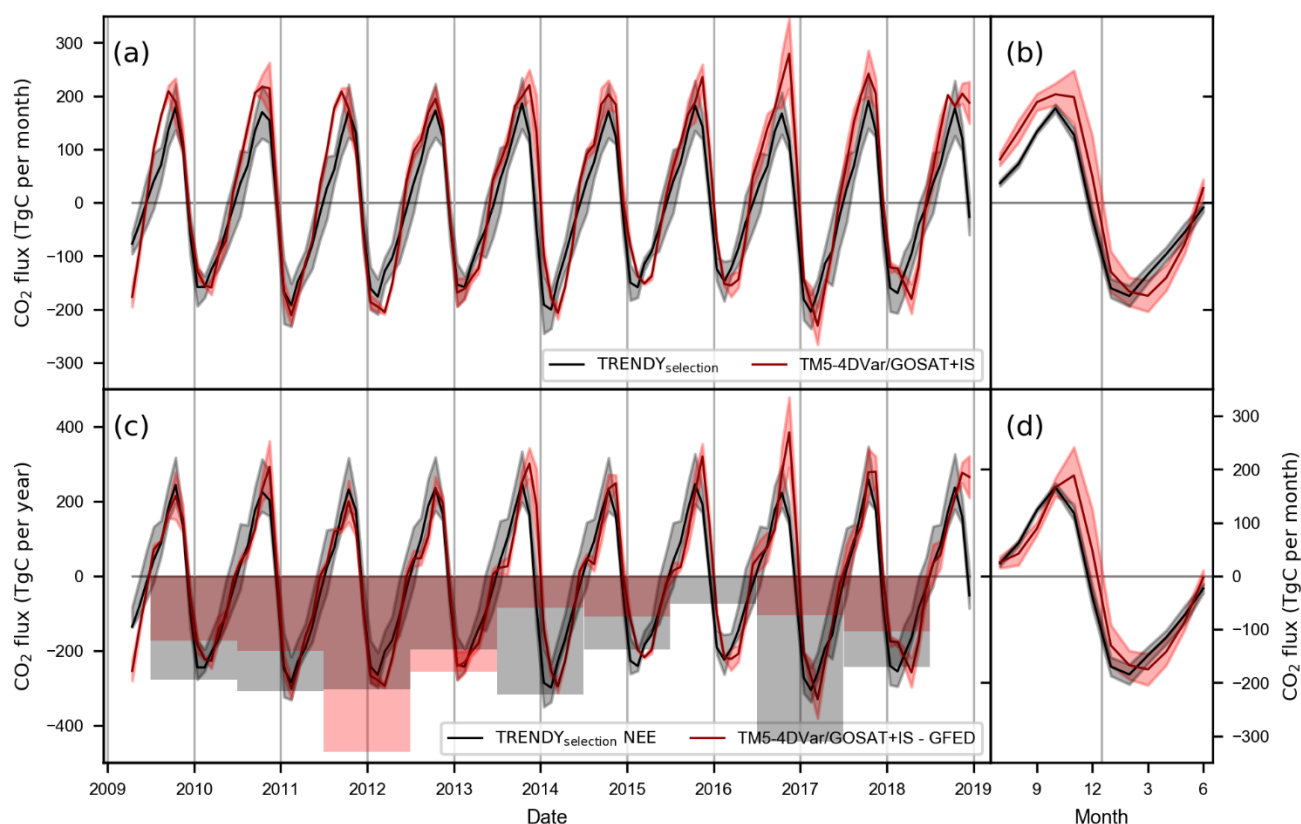
Figure 7: Annual and mean monthly NBP and NEE fluxes in southern Africa. The NBP fluxes by TM5-4DVar/GOSAT+IS (red)
290   **and selected TRENDY models (black) are given as mean monthly fluxes in Panel (a) and as the mean seasonal cycle in Panel (b).**
Similar to that, Panel (c) and (d) show the monthly NEE fluxes (GFED is subtracted from TM5-4DVar/GOSAT+IS). Additionally,
the annual (July to June) NEE fluxes of the selected TRENDY models and TM5-4DVar/GOSAT+IS – GFED fluxes are given. The
shading indicates the standard deviation over the TRENDY models and range of TM5-4DVar/ACOS+IS and TM5-
295   **4DVar/RemoTeC+IS (Panel (a) and (c)) and over the years (Panel (b) and (d)).**

Panel (c) in Fig. 7 additionally shows the annual NEE fluxes (July-June) as bars. The absolute difference between TM5-4DVar/GOSAT+IS and TRENDY annual fluxes is large in some years. These differences are caused by a stronger sink at the beginning of 2012 and enhanced emissions at the end of 2013 and 2016 in TM5-4DVar/GOSAT+IS compared to TRENDY.

However, while both datasets do not agree on the absolute value of annual fluxes in most of the years, they show a similar
IAV. Both datasets show a slightly stronger CO_2 uptake from 2010 to 2012. These years were strong and moderate La Nina
years with enhanced rainfall in 2010 and 2011 in the study region compared to the longtime mean (see Fig. A5).
Additionally, lower than average temperatures led to enhanced surface near soil moisture in 2010/11. The soil moisture
declined in 2012 to reach the long-term average. In 2015 and 2016, the sink given by the GOSAT and TRENDY selection
NEE fluxes is small. These two years have been a weak and a strong El Nino year respectively with dry conditions and in
case of 2016 exceptionally high temperatures (see Fig. A5). These findings agree well with results from Pan et al. (2020)
pointing out that temperature and precipitation extremes impact the African ecosystems heavily and therefore play a key role
in the African carbon fluxes.

To conclude, especially the monthly NEE and NBP fluxes, but also the IAV of the selected TRENDY models agree well
with TM5-4DVar/GOSAT+IS NEE and NBP – although the latter was not a criterion in the selection process of the
TRENDY models. This suggests that the selected models indeed capture the carbon cycle dynamics even on a decadal time
scale. For this reason, we use the model selection for further investigations of vegetation processes driving the southern
African carbon cycle.

3.4 Seasonal and IAV of TRENDY gross fluxes
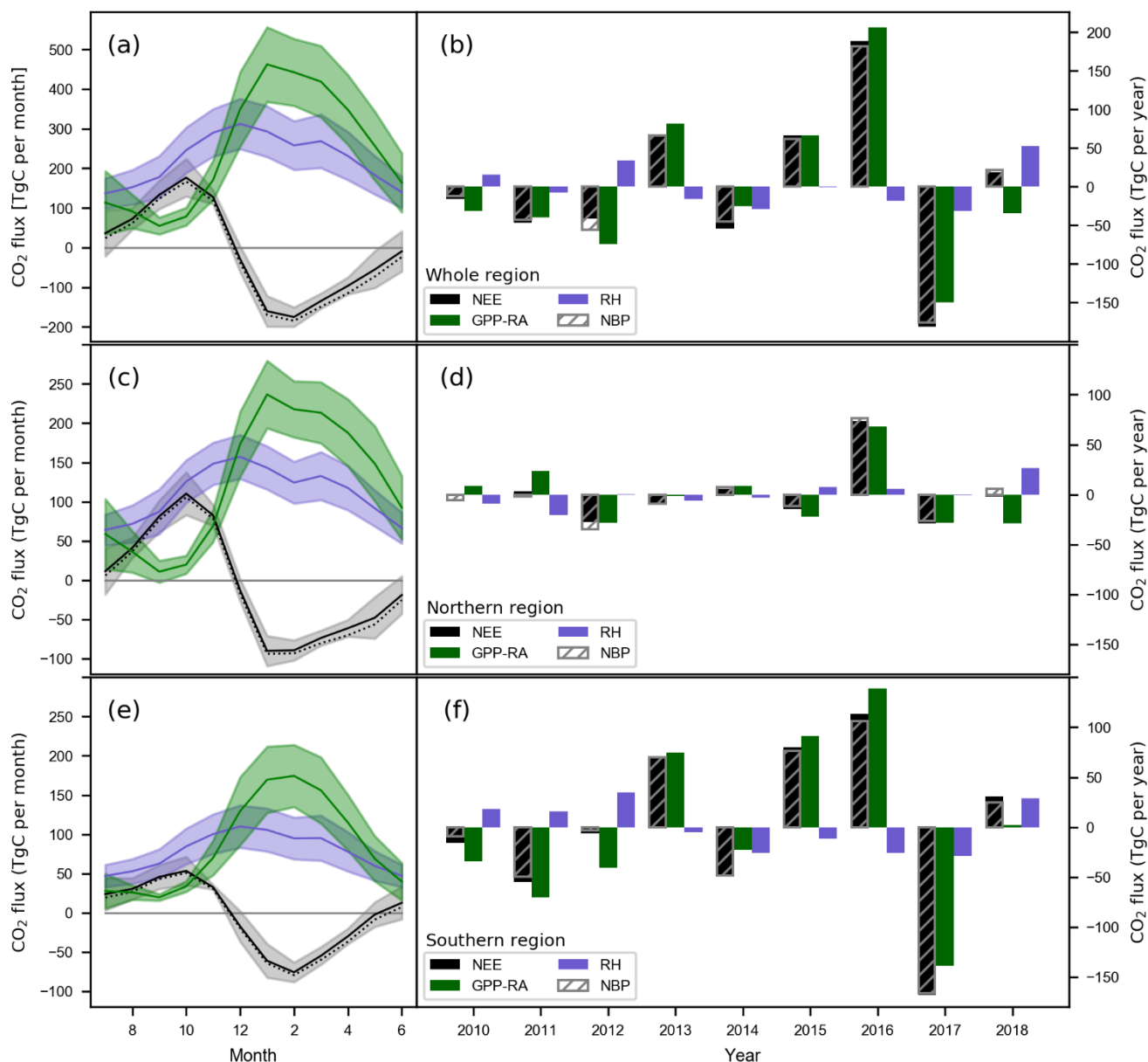
Figure 8: Annual and mean monthly CO₂ net and gross fluxes. The mean monthly fluxes (Panel (a), (c), (e)) and annual anomalies (Panel (b), (d), (f)) of NBP, NEE, GPP-RA, and RH of the selected TRENDY models are given in black, grey (dotted), green, and blue, respectively. The fluxes are given for the whole study region (Panel (a) and (b)), the Savanna dominated northern region (north of 17°S, Panel (c) and (d)), and the southern region with grass- and shrubland (Panel (e) and (f)). The annual anomalies are calculated by subtracting the individual long-term mean of the annual fluxes. Thereby, a positive GPP anomaly denotes a reduced GPP and vice versa. The shading in Panel (a), (c), and (e) indicates the standard deviation over the three selected models (ORCHIDEE, ORCHIDEEv3, and CABLE-POP).

To investigate the vegetation dynamics shaping the seasonal cycle of the southern African CO₂ exchange fluxes, we use the selected TRENDY models to further split up the net ecosystem exchange fluxes in the gross fluxes NPP (GPP – RA) and RH. The gross and net fluxes are given as mean seasonal cycle and annual anomalies in Fig. 8. In the mean seasonal cycle for the whole study region (Panel (a)), we can see a clear difference in timing between RH and GPP-RA. RH increases early in September and October, while RA increases one to two months later simultaneously with GPP (see Fig. A6). The dephasing between RH and GPP-RA leads to a prolonged emission phase in the net CO₂ exchange. It takes place in the whole region and occurs in the savanna dominated north (Fig. 8 Panel (c)) and in the grass- and shrublands in the south (Panel (e)). The dephasing takes place in every year (see Fig. A7) and is present in all selected TRENDY models. It causes a mean CO₂ release of 494 TgC during the emission phase, which is about 17% and 18% of the annual total RH and GPP-RA, respectively.

When looking at the monthly precipitation over the study region (see Fig. A8) one can identify a distinct drought phase occurring in the whole study region. The subsequent start of the rainy season in September and October temporally coincides with the early increase in RH. This finding resembles the results of Metz et al. (2023) in Australia, describing an increase of soil respiration with the beginning of the rainy season prior to the start of the growing season. The study finds soil respiration pulses resulting from rewetting of soils to cause the continental scale increase of soil respiration. Such soil respiration pulses at local arid sites are discussed in the context of Birch effect (Birch et al., 1964; Jarvis et al., 2007). Thereby the rewetting of the soil enables microbial populations to grow and to transform the carbon stored in the soils into CO₂ emissions. CO₂ is then released in substantial amounts within a short period of time. Like in Metz et al. (2023), we find short duration emission pulses in the daily flux record of a FLUXNET station in the study region. Exemplary annual records of the FLUXNET station in the Kruger National Park (Archibald et al., 2009) show CO₂ emission caused by precipitation pulses (see Fig. A9). This is also reported in Fan et al. (2015) studying a two-year measurement record of carbon fluxes in Kruger National Park in more detail. The study finds recurring respiration emission pulses due to precipitation events and attributes them to the Birch effect. The TM5-4DVar/GOSAT+IS fluxes indicate an even larger time lag between the increase of soil respiration and NPP in some years compared to TRENDY. A by 1–2 months prolonged emission phase (see Figure 7, Panel (c)) takes place in years with especially low soil moisture (2013, 2015, 2016, see Fig. A5). This later drop in emissions could either be caused by a delayed start of the GPP rise in the growing season or enhanced soil respiration due to the drier conditions. It is not possible to investigate this further, as none of the TRENDY DGVMs captured the IAV in the timing of the emission phase.

Looking at the annual gross flux anomalies given by the TRENDY selection (Fig. 8, Panel (b)), we see that the IAV of NBP and NEE is driven by GPP mainly. Enhanced GPP from 2010 to 2012 leads to a constant stronger uptake of CO₂. In 2017 a strongly enhanced GPP causes a large CO₂ sink. Reduced GPP in 2013, 2015, and 2016 results in positive NEE anomalies associated with a reduced sink in NEE. RH only plays a minor role and mostly slightly counteracts the GPP anomalies. This is in contrast to semi-arid Australia, where Metz et al. (2023) found large IAV of RH driven by precipitation anomalies during the dry season. The African study region, however, has a distinct and regular dry season every year (see Fig. A8),

355   leading to a smaller influence of RH on IAV. Note that in 2017, GOSAT suggests a much smaller annual CO_2 sink. However, the discrepancy is mainly caused by a significant difference in the emissions in the second half of the year and while both datasets agree well in the phase of carbon uptake (see Fig. 7, Panel (c)). Therefore, the TM5-4DVar/GOSAT+IS fluxes support the large GPP anomaly given by the TRENDY models but suggest stronger respiration or fire fluxes at the end of 2016. Looking at the subregions (Panels (d) and (f)), one can see that the sinks in 2010-2012 and 2017 are mainly
360   driven by the southern grassland region, whereas the comparably large release in 2016 seems to be driven by the whole African region. These findings agree with the studies of Ciais et al. (2009), Weber et al. (2009), and Williams et al. (2008) which identify GPP variability as a major source of African fluxes' IAV.

4 Conclusions

The sparsity of in situ CO_2 concentration and flux measurements cause large uncertainties in carbon flux estimates in the
365   southern African region. We show that satellite measurements provide additional information leading to an improvement of our knowledge about the southern African carbon cycle. Our study demonstrates that satellite measurement based atmospheric inversions and SIF can be used as atmospheric constraints for sub-selecting TRENDY DGVMs. This is necessary as TRENDY flux estimates show a large spread in our study region.

Using the selection of TRENDY DGVMs, we find that IAV of NBP and NEE in southern Africa is driven by GPP
370   variability. Thereby, enhancements in annual GPP mainly originate in the grass- and shrublands in the southern part of the study region. The seasonal variability of the southern African carbon fluxes is impacted by soil respiration dynamics, which are driven by the onset of the rainy season. Respiration pulses have been reported under the term of the Birch effect for arid Africa (Fan et al., 2015) and have been shown to be relevant on continental scale in semi-arid Australia (Metz et al., 2023). This enforces the relevance of rain induces CO_2 emissions for the southern African region and semi-arid regions in general.
375   Our results emphasize the importance of correctly representing the response of semi-arid ecosystems to soil rewetting in DGVMs.

380

Appendix A
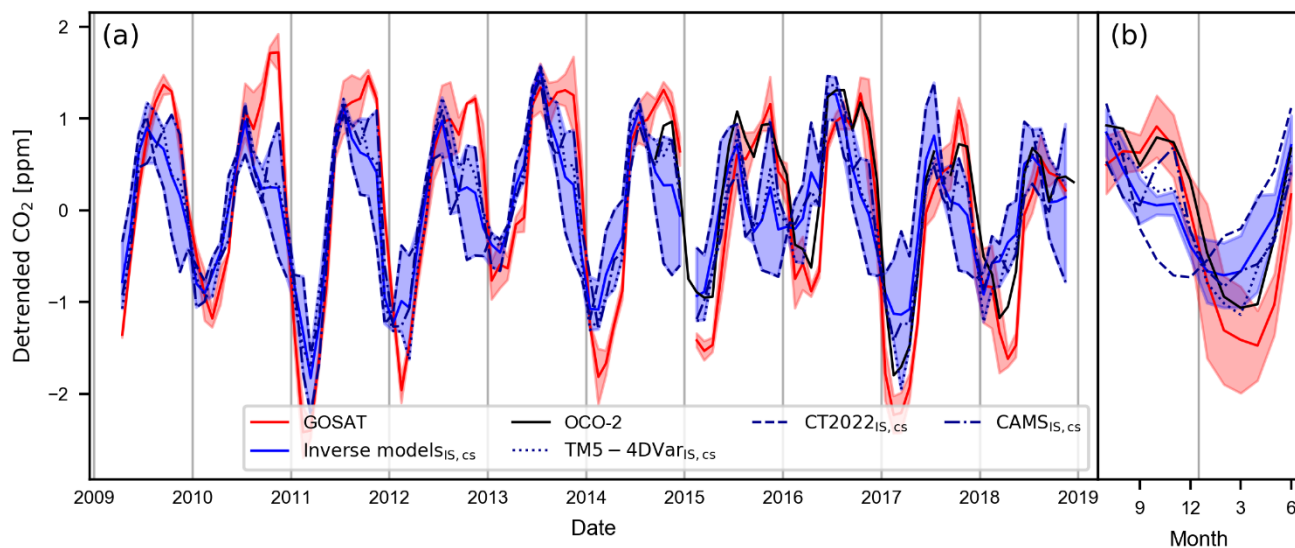
Figure A1: Monthly southern African detrended CO₂ concentrations given by inversions and satellites. Like Fig. 1, but with
385 **detrended XCO₂ measurements of OCO-2 in black und individual in-situ-only inversions co-sampled on the GOSAT measurements in dark blue (CT2022 dashed, CAMS dash-dotted, and TM5-4DVar/IS dotted). Panel (a) gives the monthly mean CO₂ concentrations, while Panel (b) shows the mean seasonal cycle 2015-2018. The shading indicates the range among GOSAT/ACOS and GOSAT/RemoTeC and the range among the three in-situ-only inversions in Panel (a). In Panel (b) the shading indicates the standard deviation over the year.**

390
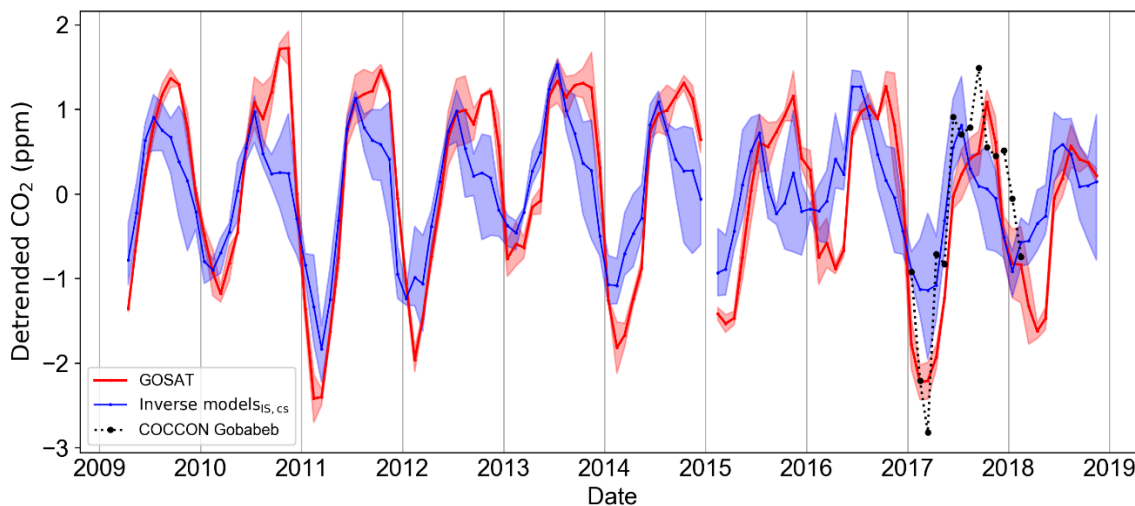
Figure A2: Monthly southern African detrended CO₂ concentrations given by inversions, satellites and COCCON measurements. Like Fig. 1, but with detrended XCO₂ measurements of the COCCON stations Gobabeb in black.
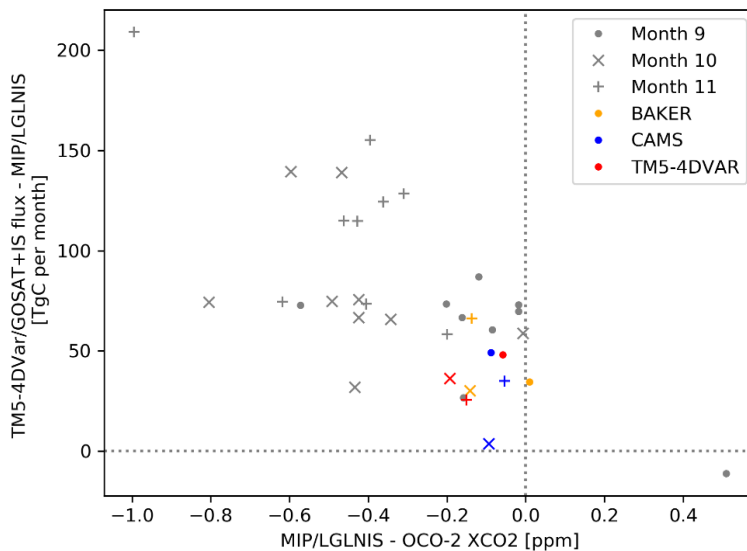
Figure A3: Performance of the individual MIP models. For the MIP/OCO-2+IS inversions 5% of the OCO-2 measurements are withheld for validation purposes and modelled XCO₂ co-sampled on the measurements are provided for each model but CSU. The mean differences of the OCO-2 measurements and modelled co-samples for each month and model are plotted against the difference of the monthly TM5-4DVar/GOSAT+IS and individual MIP/OCO-2+IS CO₂ flux. The MIP models Baker, CAMS and TM5-4DVar are highlighted in yellow, blue and red.
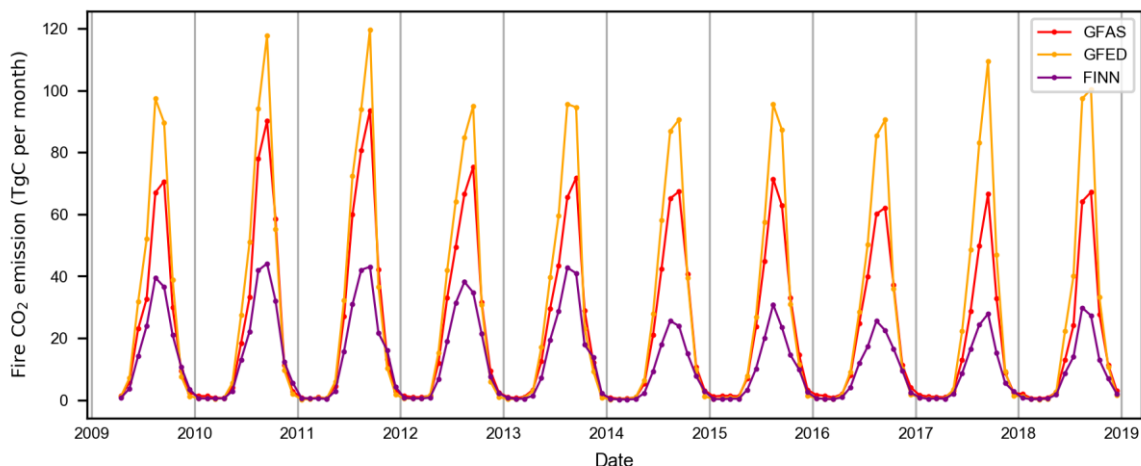
Figure A4: CO₂ fire emissions in southern Africa. The monthly CO₂ fire emissions collected by three fire emission databases
400 **(GFED in orange, Global Fire Assimilation System (GFAS (Kaiser et al., 2012)) in red and the Fire INventory from NCAR (FINN**
(Wiedinmyer et al., 2011)) in purple).
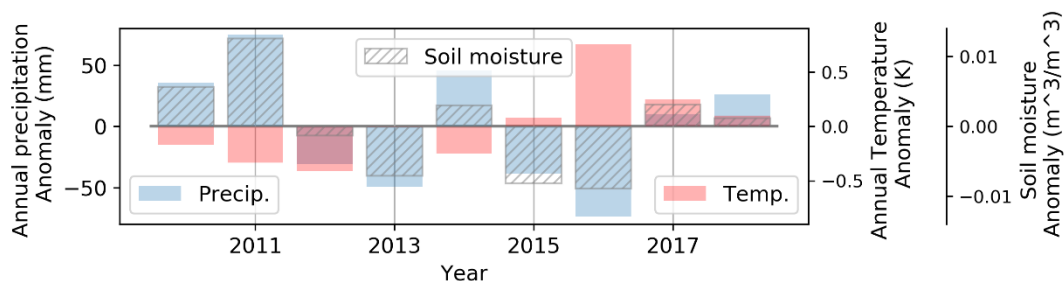
Figure A5: Climate Anomalies. The annual anomalies of ERA5 precipitation, temperature and upper layer soil moisture are given
in blue, red, and grey hashed. The annual anomalies are calculated by subtracting the individual long-term mean of the annual
values.
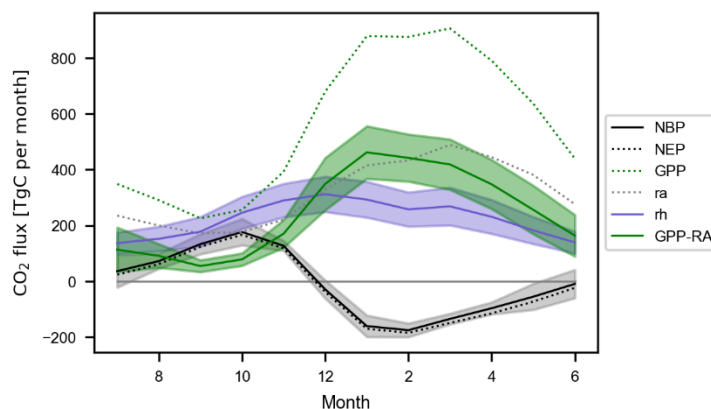
405 **Figure A6: Mean monthly CO₂ net and gross fluxes. Like Fig. 8 (a) but additionally with GPP and RA of the TRENDY selection.**
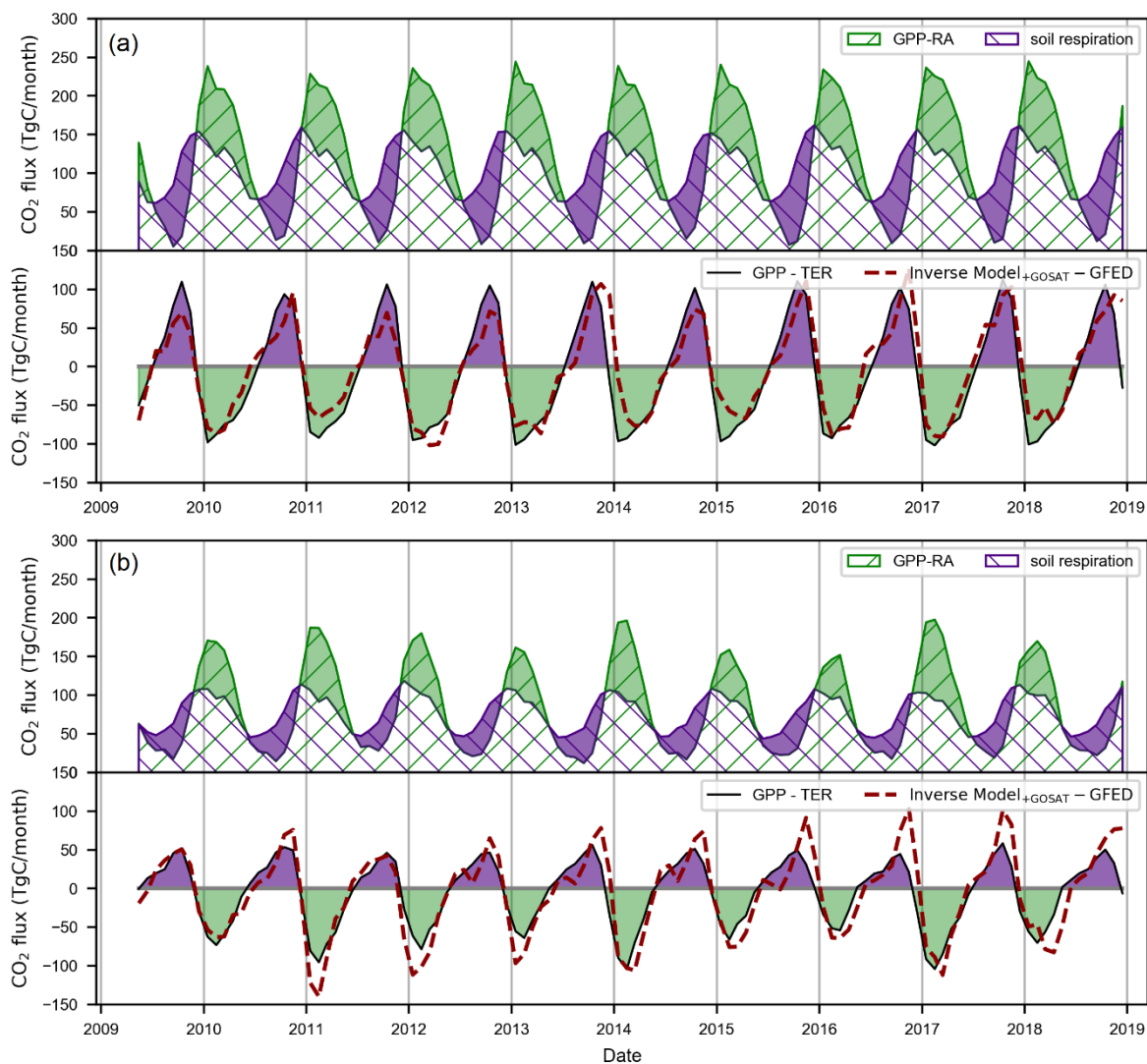
Figure A7: Monthly CO₂ fluxes in northern (Panel (a)) and southern (Panel (b)) subregion. The monthly NEE, NPP (GPP-RA), and RH fluxes from the selected TRENDY models are given in black, green, and violet respectively for the northern southern African region in Panel (a). The TM5-4DVar/GOSAT+IS - GFED NEE fluxes are additionally shown in red dotted. The same is given in Panel (b) for the southern subregion.
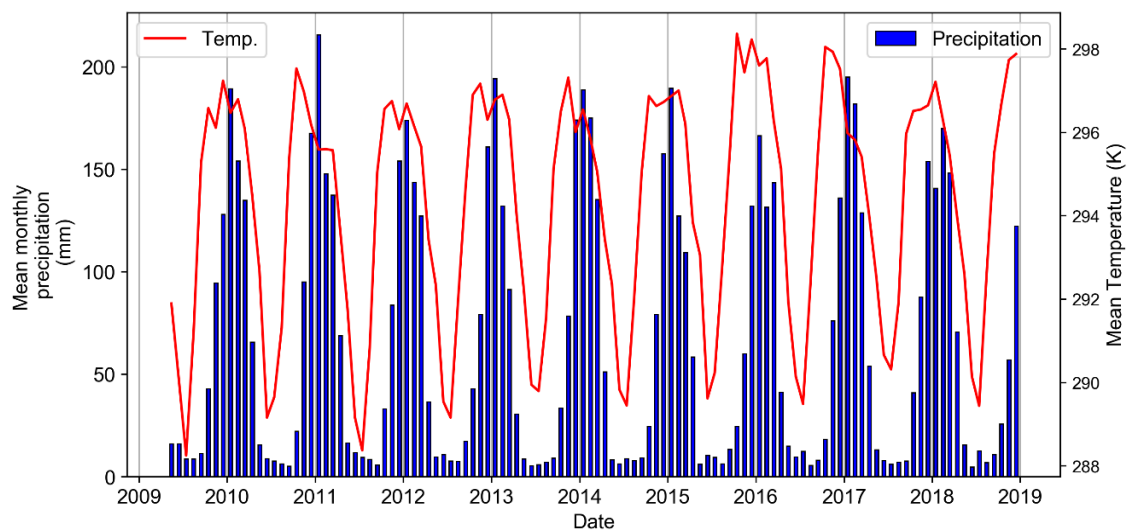
Figure A8: Monthly precipitation and temperature as mean over southern Africa. The monthly precipitation is given as blue bars and the mean temperature as solid red line.
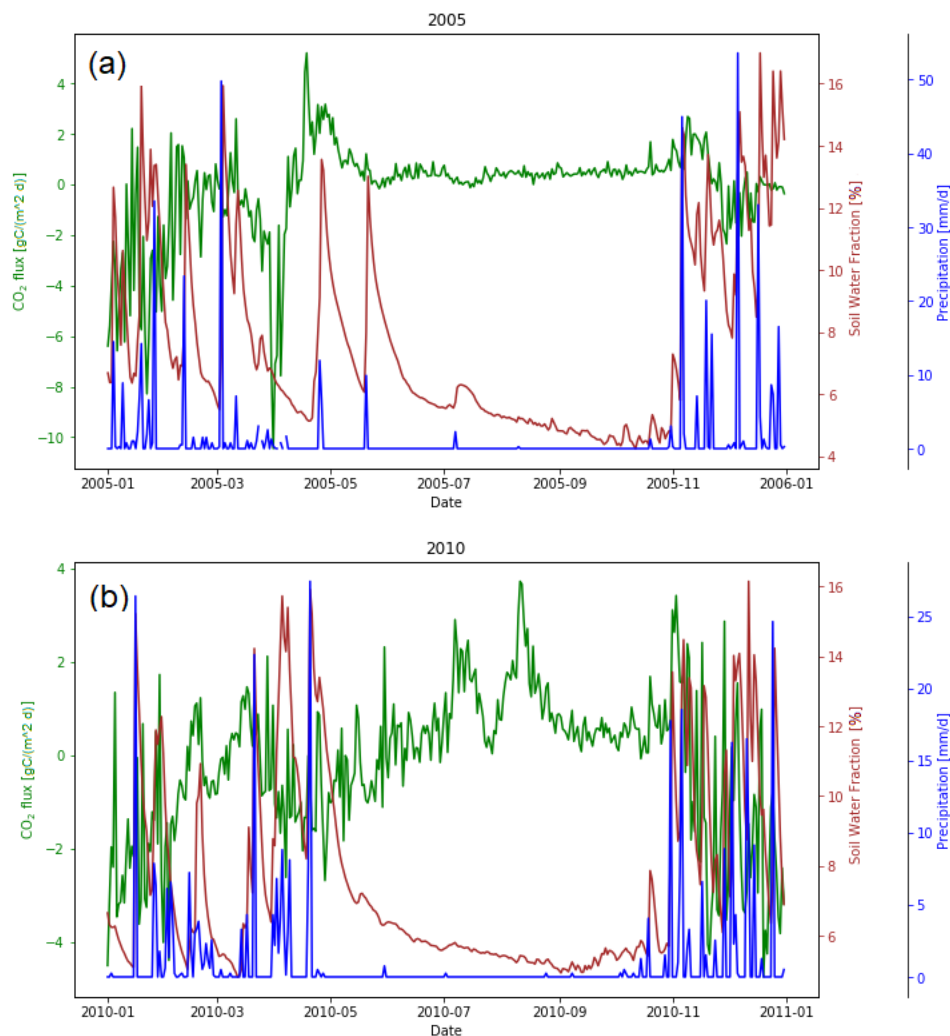
Figure A9: Local data from FLUXNET eddy covariance flux tower in Kruger National Park. Daily mean net carbon fluxes (green), precipitation (blue) and soil moisture (red) measured by the FLUXNET station ZA-Kru (Archibald et al., 2009). Panel (a) shows the year 2005, Panel (b) shows 2010.

Table A1: Summary of datasets

Description	Dataset	Resolution	References
GOSAT XCO$_2$	GOSAT/RemoTeC v2.4.0 GOSAT/ACOS v9r(Lite)	10.5 km footprint 10.5 km footprint	Butz et al., 2011, 2022 Taylor et al., 2022, OCO-2 Science Team, 2019
Validation XCO$_2$	OCO-2 v11r COCCON Gobabeb	1.3×2.3 km footprint local	Eldering et al., 2017, OCO-2/OCO-3 Science Team, 2020 Frey et al., 2021, Dubravica, 2021
Model XCO$_2$ based on in-situ data	TM5 − 4DVAR/IS CarbonTracker CT2022 CAMS v21r1	3°×2°, monthly 3°×2°, monthly 3.7°×1.81°, monthly	Basu et al., 2013 Peters et al., 2007; Jacobson et al., 2023 Chevallier et al., 2005, 2010, 2019
In-situ-only inversions	TM5 − 4DVAR/IS CarbonTracker CT2022 CAMS v20r1	3°×2°, monthly 1°×1°, monthly 3.7°×1.81°, monthly	Basu et al., 2013 Peters et al., 2007; Jacobson et al., 2023 Chevallier et al., 2005, 2010, 2019
TM5-4DVar/GOSAT+IS	TM5-4DVar/RemoTeC+IS and TM5-4DVar/ACOS+IS	3°x2°, monthly	Basu et al., 2013
TM5-4DVar/OCO-2+IS	TM5-4DVar of MIP/LNLGIS	1°x1°, monthly	Basu et al., 2013; Byrne et al., 2023
MIP/OCO-2+IS MIP/IS	MIP/LNLGIS experiment MIP/IS experiment	1°x1°, monthly	Byrne et al., 2023
SIF	GOME-2 Daily_Averaged_SIF	40 km x 40 km/80 km	Joiner et al., 2023
FLUXCOM + GFED	FLUXCOM NEE GFED v4.1s	0.08°×0.08°, 8-days 0.25°×0.25°, monthly	Tramontana et al., 2016; Jung et al., 2020 Van der Werf et al., 2017
TRENDY$_{selection}$ TRENDY$_{others}$	ORCHIDEE S3 ORCHIDEEv3 S3 CABLE-POP S3 YIBs S3 OCN S3 ORCHIDEE-CNP S3 JSBACH S3 CLASSIC S3 LPJ S3 CLM5.0 S3 DLEM S3 IBIS S3 ISAM S3 ISBA-CTRIP S3 JULES-ES-1.0 S3 LPX-Bern S3 SDGVM S3 VISIT S3	0.5°x0.5° [1] 2°x2° [1] 1°x1° [1] 1°x1° [1] 1°x1° [1] 2°x2° [1] 1.86°x1.88° [1] 2.80°x2.81° [1] 0.5°x0.5° [1] 0.94°x1.25° [1] 0.5°x0.5° [1] 1°x1° [1] 0.5°x0.5° [1] 1°x1° [1] 1.25°x1.88° [1] 0.5°x0.5° [1] 1°x1° [1] 0.5°x0.5° [1]	Krinner et al., 2005 Vuichard et al., 2019 Haverd et al., 2018 Yue and Unger, 2015 Zaehle et al., 2010 Goll et al., 2018 Reick et al., 2021 Melton et al., 2020 Poulter et al., 2011 Lawrence et al., 2019 Tian et al., 2015 Yuan et al., 2014 Meiyppan et al., 2015 Delire et al., 2020 Sellar et al., 2019 Lienert and Joos, 2018 Walker et al., 2017 Kato et al., 2013
ERA5 meteorological data	ERA5-land data total precipitation, upper layer soil moisture, temperature	1°×1°, monthly	Muñoz Sabater 2019, 2021
MODIS	MODIS (MCD12C1) data	0.05°x0.05°, 2015	Friedl and Sulla-Menashe, 2022

425 [1] all TRENDY model data is provided in monthly temporal resolution

The main characteristics and references of the observation and model data are listed. Links to the datasets are provided in the

Data availability section.

Table A2: Monthly fluxes of TM5-4DVar/GOSAT+IS in southern Africa

Year	Month	RT+IS	ACOS+IS	Mean	Year	Month	RT+IS	ACOS+IS	Mean
2009	4	-157.56	-195.50	-176.53	2014	3	-218.74	-194.84	-206.79
2009	5	-83.13	-102.61	-92.87	2014	4	-160.54	-153.89	-157.21
2009	6	6.71	6.29	6.50	2014	5	-84.72	-81.25	-82.99
2009	7	93.92	109.99	101.96	2014	6	30.42	42.46	36.44
2009	8	163.05	163.17	163.11	2014	7	82.04	99.66	90.85
2009	9	219.63	198.25	208.94	2014	8	95.93	122.13	109.03
2009	10	232.99	144.91	188.95	2014	9	215.17	154.74	184.96
2009	11	140.76	88.81	114.79	2014	10	229.27	176.57	202.92
2009	12	-32.79	-44.05	-38.42	2014	11	199.23	168.02	183.62
2010	1	-144.40	-113.34	-128.87	2014	12	36.93	-35.25	0.84
2010	2	-153.14	-157.85	-155.50	2015	1	-73.64	-86.37	-80.01
2010	3	-144.99	-172.86	-158.93	2015	2	-139.19	-135.31	-137.25
2010	4	-74.81	-121.29	-98.05	2015	3	-153.79	-149.43	-151.61
2010	5	-57.83	-84.45	-71.14	2015	4	-144.28	-131.81	-138.04
2010	6	24.59	16.57	20.58	2015	5	-62.78	-63.61	-63.19
2010	7	69.44	86.01	77.73	2015	6	2.16	22.31	12.24
2010	8	129.28	152.92	141.10	2015	7	49.88	85.39	67.64
2010	9	208.69	202.44	205.57	2015	8	117.11	107.91	112.51
2010	10	239.32	194.63	216.98	2015	9	189.95	139.90	164.93
2010	11	262.58	166.15	214.37	2015	10	225.03	150.79	187.91
2010	12	57.84	-24.29	16.78	2015	11	259.19	212.22	235.70
2011	1	-189.14	-146.26	-167.70	2015	12	112.16	78.85	95.50
2011	2	-229.46	-193.03	-211.24	2016	1	-72.92	-69.47	-71.20
2011	3	-156.96	-183.26	-170.11	2016	2	-148.67	-155.69	-152.18
2011	4	-111.27	-115.31	-113.29	2016	3	-176.60	-134.03	-155.32
2011	5	-70.44	-72.17	-71.31	2016	4	-159.32	-128.91	-144.11
2011	6	22.49	39.77	31.13	2016	5	-77.83	-56.86	-67.35
2011	7	88.88	101.56	95.22	2016	6	28.77	72.38	50.58
2011	8	170.18	183.09	176.63	2016	7	61.68	117.42	89.55
2011	9	214.57	202.08	208.32	2016	8	111.76	166.74	139.25
2011	10	215.25	137.67	176.46	2016	9	178.65	176.21	177.43
2011	11	108.61	83.75	96.18	2016	10	278.49	178.25	228.37
2011	12	-69.23	-42.93	-56.08	2016	11	344.93	213.55	279.24
2012	1	-198.76	-174.22	-186.49	2016	12	126.39	48.90	87.64
2012	2	-204.51	-185.68	-195.09	2017	1	-141.60	-144.98	-143.29
2012	3	-201.66	-209.21	-205.43	2017	2	-218.16	-157.23	-187.70
2012	4	-157.34	-149.79	-153.56	2017	3	-266.37	-195.15	-230.76
2012	5	-85.64	-61.66	-73.65	2017	4	-171.98	-145.48	-158.73
2012	6	26.99	55.95	41.47	2017	5	-87.55	-94.62	-91.09
2012	7	81.80	111.87	96.84	2017	6	-4.45	17.30	6.43
2012	8	105.47	131.05	118.26	2017	7	36.00	108.33	72.17
2012	9	182.86	156.69	169.77	2017	8	125.62	175.62	150.62
2012	10	216.78	172.23	194.51	2017	9	191.89	212.30	202.10
2012	11	130.49	155.95	143.22	2017	10	285.32	197.40	241.36
2012	12	-29.84	-24.57	-27.20	2017	11	233.14	175.95	204.54
2013	1	-195.13	-142.42	-168.78	2017	12	3.21	3.05	3.13
2013	2	-181.41	-141.65	-161.53	2018	1	-131.45	-111.65	-121.55
2013	3	-150.87	-134.34	-142.60	2018	2	-119.89	-127.09	-123.49
2013	4	-133.19	-113.00	-123.10	2018	3	-167.60	-135.00	-151.30
2013	5	-72.44	-40.57	-56.51	2018	4	-208.14	-153.04	-180.59
2013	6	34.37	52.38	43.38	2018	5	-137.36	-102.90	-120.13
2013	7	64.78	85.80	75.29	2018	6	-21.20	23.47	1.14
2013	8	96.91	130.53	113.72	2018	7	29.86	98.30	64.08
2013	9	176.64	185.33	180.99	2018	8	110.99	163.25	137.12
2013	10	219.32	178.29	198.80	2018	9	202.02	201.28	201.65
2013	11	249.06	191.11	220.08	2018	10	182.51	179.17	180.84
2013	12	202.08	64.14	133.11	2018	11	223.74	184.91	204.33
2014	1	-79.09	-119.87	-99.48	2018	12	226.30	148.33	187.31
2014	2	-187.16	-169.20	-178.18					

The monthly fluxes of TM5-4DVar/RemoTeC+IS ('RT+IS'), TM5-4DVar/ACOS+IS (ACOS+IS), and the mean of both is
430 given in TgC/month for the whole study region.

Data availability. GOSAT/RemoTeC2.4.0 XCO$_2$ data can be obtained from Zenodo https://doi.org/10.5281/zenodo.7648699 (Butz, 2022) (last access: 2024-05-15). GOSAT/ACOS data are available at https://oco2.gesdisc.eosdis.nasa.gov/data/GOSAT_TANSO_Level2/ACOS_L2_Lite_FP.9r/ (last access: 2020-07-28). OCO-2 data are available at https://disc.gsfc.nasa.gov/datasets/OCO2_L2_Standard_11r/summary (last access: 2023-06-28).

435 CarbonTracker CT2022 CO$_2$ fluxes and concentrations can be downloaded from https://gml.noaa.gov/aftp/products/carbontracker/co2/CT2022/fluxes/monthly/ (last access: 2023-04-17) and https://gml.noaa.gov/aftp/products/carbontracker/co2/CT2022/molefractions/co2_total_monthly/ (last access: 2024-06-07), respectively. CAMS concentrations and fluxes can be found at https://ads.atmosphere.copernicus.eu/cdsapp#!/dataset/cams-global-greenhouse-gas-inversion (last access: 2021-10-07). GFAS emissions records are available at https://apps.ecmwf.int/

440 datasets/data/cams-gfas/ (last access: 2020-11-13). CAMS and GFAS data were generated using Copernicus Atmosphere Service Information [2021], and neither the European Commission nor the European Centre for Medium-Range Weather Forecasts (ECMWF) is responsible for any use that may be made of the information it contains. The MIP data can be downloaded from https://www.gml.noaa.gov/ccgg/OCO2_v10mip/ (last access: 2022-05-06). GFED fire emissions are available at https://www.geo.vu.nl/~gwerf/GFED/GFED4/ (last access: 2020-07-10). FINN data were retrieved from the

445 American National Center for Atmospheric Research https://www2.acom.ucar.edu/modeling/finn-fire-inventory-ncar (last access: 2020-11-18). ERA5-land data records contain modified Copernicus Atmosphere Service Information [2021] available at the Climate Data Store https://cds.climate.copernicus.eu/cdsapp#!/dataset/reanalysis-era5-land-monthly-means (last access: 2023-10-13). TRENDYv9 model output and FLUXCOM products are available at https://sites.exeter.ac.uk/trendy and http://fluxcom.org/CF-Download/, respectively. Data of the FLUXNET station ZA-Kru

450 can be downloaded from the FLUXNET webpage: https://fluxnet.org/data/fluxnet2015-dataset/ (last access 21.11.2023). COCCON Gobabeb station data is available at https://secondary-data-archive.nilu.no/evdc/ftir/coccon/gobabeb/version2/ (last access: 2023-03-27). MODIS MCD12C1 data is available on https://search.earthdata.nasa.gov/search with the DOI 10.5067/MODIS/MCD12C1.061 (last access: 2024-03-24). L2 Daily Solar-Induced Fluorescence (SIF) from MetOp-A GOME-2 V2 data is available at from https://search.earthdata.nasa.gov/ (last access 2024-05-29). Monthly TM5-4DVAR

455 data are available in Table A2.

Code availability: The code used in this study is available at https://zenodo.org/doi/10.5281/zenodo.12528504 or GitHub (https://github.com/ ATMO-IUP-UHEI/MetzEtAl2024)

460 *Competing interests*. The authors declare that they have no conflict of interest.

Author contributions. S.N.V., A.B. and E.-M.M. were involved in conceptualization and methodology. S.B. performed the dedicated TM5-4DVAR runs. E.-M.M. conducted the formal analysis and the visualization under the supervision of A.B.

and S.N.V. E.-M.M. wrote the original draft. All authors contributed to the interpretation of the results and the editing and review of the manuscript.

Funding. Funding for the developing RemoTeC was provided by the German Research Foundation (DFG) through grant BU2599/1-1, operations and data storage was supported by DFG grant INST 35/1503-1 FUGG. S.B. was supported by NASA grant 80NSSC20K0818.

Acknowledgements. We gratefully acknowledge the data storage service SDS@hd supported by the Ministry of Science, Research and the Arts Baden-Württemberg (MWK) and the computing resources provided by the DKRZ under project bb1170. E.-M.M. acknowledges a doctoral scholarship from the German National Academic Foundation. We thank the Japanese Aerospace Exploration Agency, the National Institute for Environmental Studies, and the Ministry of Environment for the GOSAT data and their continuous support as part of the Joint Research Agreement. We thank the OCO-2 science team for producing the GOSAT/ACOS L2 XCO_2 data. OCO-2 data were produced by the OCO-2 project at the Jet Propulsion Laboratory, California Institute of Technology, and obtained from the OCO-2 data archive maintained at the NASA Goddard Earth Science Data and Information Services Center. CarbonTracker CT2022 results were provided by NOAA ESRL, Boulder, Colorado, USA, from the website at http://carbontracker.noaa.gov. We thank Stephen Sitch, Pierre Friedlingstein, and all modellers of the Trends in Net Land-Atmosphere Exchange project (TRENDY; https://blogs.exeter.ac.uk/trendy/). The long-term operation of the COCCON Gobabeb site in Namibia is supported by ESA via the COCCON-PROCEEDS series of projects (contract no. 4000121212) and COCCON-OPERA (contract no. 4000140431/23/I-DT-Ir).

References

Ahlström, A., Raupach, M. R., Schurgers, G., Smith, B., Arneth, A., Jung, M., Reichstein, M., Canadell, J. G., Friedlingstein, P., Jain, A. K., Kato, E., Poulter, B., Sitch, S., Stocker, B. D., Viovy, N., Wang, Y. P., Wiltshire, A., Zaehle, S., and Zeng, N.: The dominant role of semi-arid ecosystems in the trend and variability of the land CO_2 sink, Science, 348, 895–899, doi:10.1126/science.aaa1668, 2015.

Archibald, S. A., Kirton, A., van der Merwe, M. R., Scholes, R. J., Williams, C. A., and Hanan, N.: Drivers of inter-annual variability in Net Ecosystem Exchange in a semi-arid savanna ecosystem, South Africa, Biogeosciences, 6, 251–266, doi:10.5194/bg-6-251-2009, 2009.

Bastos, A., O'Sullivan, M., Ciais, P., Makowski, D., Sitch, S., Friedlingstein, P., Chevallier, F., Rödenbeck, C., Pongratz, J., Luijkx, I. T., Patra, P. K., Peylin, P., Canadell, J. G., Lauerwald, R., Li, W., Smith, N. E., Peters, W., Goll, D. S., Jain, A. K., Kato, E., Lienert, S., Lombardozzi, D. L., Haverd, V., Nabel, J. E. M. S., Poulter, B., Tian, H., Walker, A. P., and Zaehle, S.: Sources of Uncertainty in Regional and Global Terrestrial CO_2 Exchange Estimates, Global Biogeochem. Cycles, 34, e2019GB006393, doi:10.1029/2019GB006393, 2020.

Basu, S., Guerlet, S., Butz, A., Houweling, S., Hasekamp, O., Aben, I., Krummel, P., Steele, P., Langenfelds, R., Torn, M., Biraud, S., Stephens, B., Andrews, A., and Worthy, D.: Global CO_2 fluxes estimated from GOSAT retrievals of total column CO_2: exit, Atmos. Chem. Phys., 13, 8695–8717, doi:10.5194/acp-13-8695-2013, 2013.

Birch, H. F.: Mineralisation of plant nitrogen following alternate wet and dry conditions, Plant Soil, 20, 43–49, doi:10.1007/bf01378096, 1964.

Butz, A., Guerlet, S., Hasekamp, O., Schepers, D., Galli, A., Aben, I., Frankenberg, C., Hartmann, J.-M., Tran, H., Kuze, A., Keppel-Aleks, G., Toon, G., Wunch, D., Wennberg, P., Deutscher, N., Griffith, D., Macatangay, R., Messerschmidt, J., Notholt, J., and Warneke, T.: Toward accurate CO_2 and CH_4 observations from GOSAT, Geophys. Res. Lett., 38, n/a-n/a, doi:10.1029/2011GL047888, 2011.

Butz, A.: RemoTeC full-physics retrieval GOSAT/TANSO-FTS Level 2 bias-corrected XCO_2 version 2.4.0 operated at Heidelberg University [data set], doi:10.5281/zenodo.5886662, 2022.

Byrne, B., Baker, D. F., Basu, S., Bertolacci, M., Bowman, K. W., Carroll, D., Chatterjee, A., Chevallier, F., Ciais, P., Cressie, N., Crisp, D., Crowell, S., Deng, F., Deng, Z., Deutscher, N. M., Dubey, M. K., Feng, S., García, O. E., Griffith, D. W. T., Herkommer, B., Hu, L., Jacobson, A. R., Janardanan, R., Jeong, S., Johnson, M. S., Jones, D. B. A., Kivi, R., Liu, J., Liu, Z., Maksyutov, S., Miller, J. B., Miller, S. M., Morino, I., Notholt, J., Oda, T., O'Dell, C. W., Oh, Y.-S., Ohyama, H., Patra, P. K., Peiro, H., Petri, C., Philip, S., Pollard, D. F., Poulter, B., Remaud, M., Schuh, A., Sha, M. K., Shiomi, K., Strong, K., Sweeney, C., Té, Y., Tian, H., Velazco, V. A., Vrekoussis, M., Warneke, T., Worden, J. R., Wunch, D., Yao, Y., Yun, J., Zammit-Mangion, A., and Zeng, N.: National CO 2 budgets (2015–2020) inferred from atmospheric CO 2 observations in support of the global stocktake, Earth Syst. Sci. Data, 15, 963–1004, doi:10.5194/essd-15-963-2023, 2023.

Chevallier, F., Engelen, R. J., and Peylin, P.: The contribution of AIRS data to the estimation of CO_2 sources and sinks, Geophys. Res. Lett., 32, doi:10.1029/2005GL024229, 2005.

520   Chevallier, F., Ciais, P., Conway, T. J., Aalto, T., Anderson, B. E., Bousquet, P., Brunke, E. G., Ciattaglia, L., Esaki, Y., and Fröhlich, M.: CO_2 surface fluxes at grid point scale estimated from a global 21 year reanalysis of atmospheric measurements, J. Geophys. Res. Atmos., 115, doi:10.1029/2010JD013887, 2010.

Chevallier, F., Remaud, M., O'Dell, C. W., Baker, D., Peylin, P., and Cozic, A.: Objective evaluation of surface- and satellite-driven carbon dioxide atmospheric inversions, Atmos. Chem. Phys., 19, 14233–14251, doi:10.5194/acp-19-
525   14233-2019, 2019.

Ciais, P., Piao, S.-L., Cadule, P., Friedlingstein, P., and Chédin, A.: Variability and recent trends in the African terrestrial carbon balance, Biogeosciences, 6, 1935–1948, doi:10.5194/bg-6-1935-2009, 2009.

Delire, C., Séférian, R., Decharme, B., Alkama, R., Calvet, J.-C., Carrer, D., Gibelin, A.-L., Joetzjer, E., Morel, X., Rocher, M., and Tzanos, D.: The Global Land Carbon Cycle Simulated With ISBA-CTRIP: Improvements Over the Last
530   Decade, J. Adv. Model. Earth Syst., 12, doi:10.1029/2019MS001886, 2020.

Detmers, R. G., Hasekamp, O., Aben, I., Houweling, S., Leeuwen, T. T., Butz, A., Landgraf, J., Köhler, P., Guanter, L., and Poulter, B.: Anomalous carbon uptake in Australia as seen by GOSAT, Geophys. Res. Lett., 42, 8177–8184, doi:10.1002/2015GL065161, 2015.

Dubravica, D., Hase, F., Alberti, C., Frey, M., Marais, E.: COCCON Version 2 dataset from atmospheric observatory of
535   Gobabeb (Namibia) available at the EVDC Data Handling Facilities covering start date Jan 9th 2017 to end date Nov 27th 2020, COCCON - Central Facility / EVDC - ESA Atmospheric Validation Data Centre [data set], doi:10.48477/coccon.pfl0.gobabeb.R02, 2021.

Edwards, D. P., Emmons, L. K., Gille, J. C., Chu, A., Attié, J.-L., Giglio, L., Wood, S. W., Haywood, J., Deeter, M. N., Massie, S. T., Ziskin, D. C., and Drummond, J. R.: Satellite-observed pollution from Southern Hemisphere biomass
540   burning, J. Geophys. Res., 111, doi:10.1029/2005JD006655, 2006.

Eldering, A., Wennberg, P. O., Crisp, D., Schimel, D. S., Gunson, M. R., Chatterjee, A., Liu, J., Schwandner, F. M., Sun, Y., O'Dell, C. W., Frankenberg, C., Taylor, T., Fisher, B., Osterman, G. B., Wunch, D., Hakkarainen, J., Tamminen, J., and Weir, B.: The Orbiting Carbon Observatory-2 early science investigations of regional carbon dioxide fluxes, Science, 358, eaam5745, doi:10.1126/science.aam5745, 2017.

545   Ernst, Y., Archibald, S., Balzter, H., Chevallier, F., Ciais, P., Fischer, C. G., Gaubert, B., Higginbottom, T., Higgins, S., Lawal, S., Lacroix, F., Lauerwald, R., Lourenco, M., Martens, C., Mengistu, A. G., Merbold, L., Mitchard, E., Moyo, M., Nguyen, H., O'sullivan, M., Rodríguez-Veiga, P., Rosan, T., Rosentreter, J., Ryan, C., Scheiter, S., Sitch, S., Stevens, N., Tagesson, T., Tian, H., Wang, M., Woon, J. S., Zheng, B., Zhou, Y., and Scholes, R. J.: The African Regional Greenhouse Gases Budget (2010–2019), Global Biogeochem. Cycles, 38, doi:10.1029/2023GB008016, 2024.

550   Fan, Z., Neff, J. C., and Hanan, N. P.: Modeling pulsed soil respiration in an African savanna ecosystem, Agricultural and Forest Meteorology, 200, 282–292, doi:10.1016/j.agrformet.2014.10.009, 2015.

Foster, K. T., Sun, W., Shiga, Y. P., Mao, J., and Michalak, A. M.: Multiscale assessment of North American terrestrial carbon balance, Biogeosciences, 21, 869–891, doi:10.5194/bg-21-869-2024, 2024.

555 Frey, M., Sha, M. K., Hase, F., Kiel, M., Blumenstock, T., Harig, R., Surawicz, G., Deutscher, N. M., Shiomi, K., Franklin, J. E., Bösch, H., Chen, J., Grutter, M., Ohyama, H., Sun, Y., Butz, A., Mengistu Tsidu, G., Ene, D., Wunch, D., Cao, Z., Garcia, O., Ramonet, M., Vogel, F., and Orphal, J.: Building the COllaborative Carbon Column Observing Network (COCCON): long-term stability and ensemble performance of the EM27/SUN Fourier transform spectrometer, Atmos. Meas. Tech., 12, 1513–1530, doi:10.5194/amt-12-1513-2019, 2019.

Frey, M. M., Hase, F., Blumenstock, T., Dubravica, D., Groß, J., Göttsche, F., Handjaba, M., Amadhila, P., Mushi, R., 560 Morino, I., Shiomi, K., Sha, M. K., Mazière, M. de, and Pollard, D. F.: Long-term column-averaged greenhouse gas observations using a COCCON spectrometer at the high-surface-albedo site in Gobabeb, Namibia, Atmos. Meas. Tech., 14, 5887–5911, doi:10.5194/amt-14-5887-2021, 2021.

Friedl, M. and Sulla-Menashe, D.: MODIS/Terra+Aqua Land Cover Type Yearly L3 Global 0.05Deg CMG V061, NASA EOSDIS Land Processes Distributed Active Archive Center [data set], doi:10.5067/MODIS/MCD12C1.061, 2022.

565 Friedlingstein, P., O'sullivan, M., Jones, M. W., Andrew, R. M., Hauck, J., Olsen, A., Peters, G. P., Peters, W., Pongratz, J., Sitch, S., Le Quéré, C., Canadell, J. G., Ciais, P., Jackson, R. B., Alin, S., Aragão, Luiz E. O. C., Arneth, A., Arora, V., Bates, N. R., Becker, M., Benoit-Cattin, A., Bittig, H. C., Bopp, L., Bultan, S., Chandra, N., Chevallier, F., Chini, L. P., Evans, W., Florentie, L., Forster, P. M., Gasser, T., Gehlen, M., Gilfillan, D., Gkritzalis, T., Gregor, L., Gruber, N., Harris, I., Hartung, K., Haverd, V., Houghton, R. A., Ilyina, T., Jain, A. K., Joetzjer, E., Kadono, K., Kato, E., Kitidis, 570 V., Korsbakken, J. I., Landschützer, P., Lefèvre, N., Lenton, A., Lienert, S., Liu, Z., Lombardozzi, D., Marland, G., Metzl, N., Munro, D. R., Nabel, Julia E. M. S., Nakaoka, S.-I., Niwa, Y., O'Brien, K., Ono, T., Palmer, P. I., Pierrot, D., Poulter, B., Resplandy, L., Robertson, E., Rödenbeck, C., Schwinger, J., Séférian, R., Skjelvan, I., Smith, A. J. P., Sutton, A. J., Tanhua, T., Tans, P. P., Tian, H., Tilbrook, B., van der Werf, G., Vuichard, N., Walker, A. P., Wanninkhof, R., Watson, A. J., Willis, D., Wiltshire, A. J., Yuan, W., Yue, X., and Zaehle, S.: Global Carbon Budget 575 2020, Earth Syst. Sci. Data, 12, 3269–3340, doi:10.5194/essd-12-3269-2020, 2020.

Friedlingstein, P., O'Sullivan, M., Jones, M. W., Andrew, R. M., Bakker, D. C. E., Hauck, J., Landschützer, P., Le Quéré, C., Luijkx, I. T., Peters, G. P., Peters, W., Pongratz, J., Schwingshackl, C., Sitch, S., Canadell, J. G., Ciais, P., Jackson, R. B., Alin, S. R., Anthoni, P., Barbero, L., Bates, N. R., Becker, M., Bellouin, N., Decharme, B., Bopp, L., Brasika, I. B. M., Cadule, P., Chamberlain, M. A., Chandra, N., Chau, T.-T.-T., Chevallier, F., Chini, L. P., Cronin, M., Dou, X., 580 Enyo, K., Evans, W., Falk, S., Feely, R. A., Feng, L., Ford, D. J., Gasser, T., Ghattas, J., Gkritzalis, T., Grassi, G., Gregor, L., Gruber, N., Gürses, Ö., Harris, I., Hefner, M., Heinke, J., Houghton, R. A., Hurtt, G. C., Iida, Y., Ilyina, T., Jacobson, A. R., Jain, A., Jarníková, T., Jersild, A., Jiang, F., Jin, Z., Joos, F., Kato, E., Keeling, R. F., Kennedy, D., Klein Goldewijk, K., Knauer, J., Korsbakken, J. I., Körtzinger, A., Lan, X., Lefèvre, N., Li, H., Liu, J., Liu, Z., Ma, L., Marland, G., Mayot, N., McGuire, P. C., McKinley, G. A., Meyer, G., Morgan, E. J., Munro, D. R., Nakaoka, S.-I., 585 Niwa, Y., O'Brien, K. M., Olsen, A., Omar, A. M., Ono, T., Paulsen, M., Pierrot, D., Pocock, K., Poulter, B., Powis, C.

M., Rehder, G., Resplandy, L., Robertson, E., Rödenbeck, C., Rosan, T. M., Schwinger, J., Séférian, R., Smallman, T. L., Smith, S. M., Sospedra-Alfonso, R., Sun, Q., Sutton, A. J., Sweeney, C., Takao, S., Tans, P. P., Tian, H., Tilbrook, B., Tsujino, H., Tubiello, F., van der Werf, G. R., van Ooijen, E., Wanninkhof, R., Watanabe, M., Wimart-Rousseau, C., Yang, D., Yang, X., Yuan, W., Yue, X., Zaehle, S., Zeng, J., and Zheng, B.: Global Carbon Budget 2023, Earth Syst.

590   Sci. Data, 15, 5301–5369, doi:10.5194/essd-15-5301-2023, 2023.

Goll, D. S., Joetzjer, E., Huang, M., and Ciais, P.: Low Phosphorus Availability Decreases Susceptibility of Tropical Primary Productivity to Droughts, Geophys. Res. Lett., 45, 8231–8240, doi:10.1029/2018GL077736, 2018.

Haverd, V., Smith, B., Nieradzik, L., Briggs, P. R., Woodgate, W., Trudinger, C. M., Canadell, J. G., and Cuntz, M.: A new version of the CABLE land surface model (Subversion revision r4601) incorporating land use and land cover change,

595   woody vegetation demography, and a novel optimisation-based approach to plant coordination of photosynthesis, Geosci. Model Dev., 11, 2995–3026, doi:10.5194/gmd-11-2995-2018, 2018.

Jacobson, A. R., Schuldt, K. N., Tans, P., Arlyn Andrews, Miller, J. B., Oda, T., Mund, J., Weir, B., Ott, L., Aalto, T., Abshire, J. B., Aikin, K., Aoki, S., Apadula, F., Arnold, S., Baier, B., Bartyzel, J., Beyersdorf, A., Biermann, T., Biraud, S. C., Boenisch, H., Brailsford, G., Brand, W. A., Chen, G., Huilin Chen, Lukasz Chmura, Clark, S., Colomb, A.,

600   Commane, R., Conil, S., Couret, C., Cox, A., Cristofanelli, P., Cuevas, E., Curcoll, R., Daube, B., Davis, K. J., Wekker, S. de, Della Coletta, J., Delmotte, M., DiGangi, E., DiGangi, J. P., Di Sarra, A. G., Dlugokencky, E., Elkins, J. W., Emmenegger, L., Shuangxi Fang, Fischer, M. L., Forster, G., Frumau, A., Galkowski, M., Gatti, L. V., Gehrlein, T., Gerbig, C., Francois Gheusi, Gloor, E., Gomez-Trueba, V., Goto, D., Griffis, T., Hammer, S., Hanson, C., Haszpra, L., Hatakka, J., Heimann, M., Heliasz, M., Hensen, A., Hermansen, O., Hintsa, E., Holst, J., Ivakhov, V., Jaffe, D. A.,

605   Jordan, A., Joubert, W., Karion, A., Kawa, S. R., Kazan, V., Keeling, R. F., Keronen, P., Kneuer, T., Kolari, P., Kateřina Komínková, Kort, E., Kozlova, E., Krummel, P., Kubistin, D., Labuschagne, C., Lam, D. H., Lan, X., Langenfelds, R. L., Laurent, O., Laurila, T., Lauvaux, T., Lavric, J., Law, B. E., Lee, J., Lee, O. S., Lehner, I., Lehtinen, K., Leppert, R., Leskinen, A., Leuenberger, M., Levin, I., Levula, J., Lin, J., Lindauer, M., Loh, Z., Lopez, M., Luijkx, I. T., Lunder, C. R., Machida, T., Mammarella, I., Manca, G., Manning, A., Manning, A., Marek, M. V., Martin, M. Y., Matsueda, H.,

610   McKain, K., Meijer, H., Meinhardt, F., Merchant, L., N. Mihalopoulos, Miles, N. L., Miller, C. E., Mitchell, L., Mölder, M., Montzka, S., Moore, F., Moossen, H., Morgan, E., Josep-Anton Morgui, Morimoto, S., Müller-Williams, J., J. William Munger, Munro, D., Myhre, C. L., Shin-Ichiro Nakaoka, Jaroslaw Necki, Newman, S., Nichol, S., Niwa, Y., Obersteiner, F., O'Doherty, S., Paplawsky, B., Peischl, J., Peltola, O., Piacentino, S., Jean-Marc Pichon, Pickers, P., Piper, S., Pitt, J., Plass-Dülmer, C., Platt, S. M., Prinzivalli, S., Ramonet, M., Ramos, R., Reyes-Sanchez, E.,

615   Richardson, S. J., Riris, H., Rivas, P. P., Ryerson, T., Saito, K., Sargent, M., Sasakawa, M., Scheeren, B., Schuck, T., Schumacher, M., Seifert, T., Sha, M. K., Shepson, P., Shook, M., Sloop, C. D., Smith, P., Stanley, K., Steinbacher, M., Stephens, B., Sweeney, C., Thoning, K., Timas, H., Torn, M., Tørseth, K., Trisolino, P., Turnbull, J., van den Bulk, P., van Dinther, D., Vermeulen, A., Viner, B., Vitkova, G., Walker, S., Watson, A., Wofsy, S. C., Worsey, J., Worthy, D., Dickon Young, Zaehle, S., Zahn, A., and Miroslaw Zimnoch: CarbonTracker CT2022, doi:10.25925/z1gj-3254, 2023.

620   Jarvis, P., Rey, A., Petsikos, C., Wingate, L., Rayment, M., Pereira, J., Banza, J., David, J., Miglietta, F., Borghetti, M.,
Manca, G., and Valentini, R.: Drying and wetting of Mediterranean soils stimulates decomposition and carbon dioxide
emission: the "Birch effect", Tree Physiol. (Tree Physiology), 27, 929–940, doi:10.1093/treephys/27.7.929, 2007.

Joiner, J., Yoshida, Y., Koehler, P., Frankenberg, C., and Parazoo, N. C.: L2 Daily Solar-Induced Fluorescence (SIF) from
MetOp-A GOME-2, 2007-2018, V2, ORNL DAAC, Oak Ridge, Tennessee, USA [data set],
625   doi:10.3334/ORNLDAAC/2292, 2023.

Jung, M., Schwalm, C., Migliavacca, M., Walther, S., Camps-Valls, G., Koirala, S., Anthoni, P., Besnard, S., Bodesheim, P.,
Carvalhais, N., Chevallier, F., Gans, F., Goll, D. S., Haverd, V., Köhler, P., Ichii, K., Jain, A. K., Liu, J., Lombardozzi,
D., Nabel, Julia E. M. S., Nelson, J. A., O'Sullivan, M., Pallandt, M., Papale, D., Peters, W., Pongratz, J., Rödenbeck,
C., Sitch, S., Tramontana, G., Walker, A., Weber, U., and Reichstein, M.: Scaling carbon fluxes from eddy covariance
630   sites to globe: synthesis and evaluation of the FLUXCOM approach, Biogeosciences, 17, 1343–1365, doi:10.5194/bg-
17-1343-2020, 2020.

Kaiser, J. W., Heil, A., Andreae, M. O., Benedetti, A., Chubarova, N., Jones, L., Morcrette, J.-J., Razinger, M., Schultz, M.
G., Suttie, M., and van der Werf, G. R.: Biomass burning emissions estimated with a global fire assimilation system
based on observed fire radiative power, Biogeosciences, 9, 527–554, doi:10.5194/bg-9-527-2012, 2012.

635   Kato, E., Kinoshita, T., Ito, A., Kawamiya, M., and Yamagata, Y.: Evaluation of spatially explicit emission scenario of land-
use change and biomass burning using a process-based biogeochemical model, Journal of Land Use Science, 8, 104–
122, doi:10.1080/1747423X.2011.628705, 2013.

Krinner, G., Viovy, N., Noblet-Ducoudré, N. de, Ogée, J., Polcher, J., Friedlingstein, P., Ciais, P., Sitch, S., and Prentice, I.
C.: A dynamic global vegetation model for studies of the coupled atmosphere-biosphere system, Global Biogeochem.
640   Cycles, 19, doi:10.1029/2003GB002199, 2005.

Lasslop, G., Hantson, S., Harrison, S. P., Bachelet, D., Burton, C., Forkel, M., Forrest, M., Li, F., Melton, J. R., Yue, C.,
Archibald, S., Scheiter, S., Arneth, A., Hickler, T., and Sitch, S.: Global ecosystems and fire: Multi-model assessment of
fire-induced tree-cover and carbon storage reduction, Global Change Biology, 26, 5027–5041, doi:10.1111/gcb.15160,
2020.

645   Lawrence, D. M., Fisher, R. A., Koven, C. D., Oleson, K. W., Swenson, S. C., Bonan, G., Collier, N., Ghimire, B.,
Kampenhout, L., Kennedy, D., Kluzek, E., Lawrence, P. J., Li, F., Li, H., Lombardozzi, D., Riley, W. J., Sacks, W. J.,
Shi, M., Vertenstein, M., Wieder, W. R., Xu, C., Ali, A. A., Badger, A. M., Bisht, G., Broeke, M., Brunke, M. A., Burns,
S. P., Buzan, J., Clark, M., Craig, A., Dahlin, K., Drewniak, B., Fisher, J. B., Flanner, M., Fox, A. M., Gentine, P.,
Hoffman, F., Keppel-Aleks, G., Knox, R., Kumar, S., Lenaerts, J., Leung, L. R., Lipscomb, W. H., Lu, Y., Pandey, A.,
650   Pelletier, J. D., Perket, J., Randerson, J. T., Ricciuto, D. M., Sanderson, B. M., Slater, A., Subin, Z. M., Tang, J.,
Thomas, R. Q., Val Martin, M., and Zeng, X.: The Community Land Model Version 5: Description of New Features,
Benchmarking, and Impact of Forcing Uncertainty, J. Adv. Model. Earth Syst., 11, 4245–4287,
doi:10.1029/2018MS001583, 2019.

Li, X., Xiao, J., He, B., Altaf Arain, M., Beringer, J., Desai, A. R., Emmel, C., Hollinger, D. Y., Krasnova, A., Mammarella, I., Noe, S. M., Ortiz, P. S., Rey-Sanchez, A. C., Rocha, A. V., and Varlagin, A.: Solar-induced chlorophyll fluorescence is strongly correlated with terrestrial photosynthesis for a wide variety of biomes: First global analysis based on OCO-2 and flux tower observations, Global Change Biology, 24, 3990–4008, doi:10.1111/gcb.14297, 2018.

Lienert, S. and Joos, F.: A Bayesian ensemble data assimilation to constrain model parameters and land-use carbon emissions, Biogeosciences, 15, 2909–2930, doi:10.5194/bg-15-2909-2018, 2018.

MacBean, N., Scott, R. L., Biederman, J. A., Peylin, P., Kolb, T., Litvak, M. E., Krishnan, P., Meyers, T. P., Arora, V. K., Bastrikov, V., Goll, D., Lombardozzi, D. L., Nabel, Julia E. M. S., Pongratz, J., Sitch, S., Walker, A. P., Zaehle, S., and Moore, D. J. P.: Dynamic global vegetation models underestimate net CO_2 flux mean and inter-annual variability in dryland ecosystems, Environ. Res. Lett., 16, 94023, doi:10.1088/1748-9326/ac1a38, 2021.

Masarie, K. A., Peters, W., Jacobson, A. R., and Tans, P. P.: ObsPack: a framework for the preparation, delivery, and attribution of atmospheric greenhouse gas measurements, Earth Syst. Sci. Data, 6, 375–384, doi:10.5194/essd-6-375-2014, 2014.

Meiyappan, P., Jain, A. K., and House, J. I.: Increased influence of nitrogen limitation on CO_2 emissions from future land use and land use change, Global Biogeochem. Cycles, 29, 1524–1548, doi:10.1002/2015GB005086, 2015.

Melton, J. R., Arora, V. K., Wisernig-Cojoc, E., Seiler, C., Fortier, M., Chan, E., and Teckentrup, L.: CLASSIC v1.0: the open-source community successor to the Canadian Land Surface Scheme (CLASS) and the Canadian Terrestrial Ecosystem Model (CTEM) – Part 1: Model framework and site-level performance, Geosci. Model Dev., 13, 2825–2850, doi:10.5194/gmd-13-2825-2020, 2020.

Mengistu, A. G. and Mengistu Tsidu, G.: On the performance of satellite-based observations of XCO_2 in capturing the NOAA Carbon Tracker model and ground-based flask observations over Africa's land mass, Atmos. Meas. Tech., 13, 4009–4033, doi:10.5194/amt-13-4009-2020, 2020.

Metz, E.-M., Vardag, S. N., Basu, S., Jung, M., Ahrens, B., El-Madany, T., Sitch, S., Arora, V. K., Briggs, P. R., Friedlingstein, P., Goll, D. S., Jain, A. K., Kato, E., Lombardozzi, D., Nabel, Julia E. M. S., Poulter, B., Séférian, R., Tian, H., Wiltshire, A., Yuan, W., Yue, X., Zaehle, S., Deutscher, N. M., Griffith, D. W. T., and Butz, A.: Soil respiration-driven CO_2 pulses dominate Australia's flux variability, Science, 379, 1332–1335, doi:10.1126/science.add7833, 2023.

Muñoz Sabater, J.: ERA5-Land monthly averaged data from 1981 to present, Copernicus Climate Change Service (C3S) Climate Data Store (CDS) [data set], doi:10.24381/cds.68d2bb3, 2019.

Muñoz Sabater, J.: ERA5-Land monthly averaged data from 1981 to present, Copernicus Climate Change Service (C3S) Climate Data Store (CDS) [data set], doi:10.24381/cds.68d2bb3, 2021.

OCO-2 Science Team, Gunson M., Eldering A.:, ACOS GOSAT/TANSO-FTS Level 2 bias-corrected XCO2 and other select fields from the full-physics retrieval aggregated as daily files V9r, Greenbelt, MD, USA, Goddard Earth Sciences Data and Information Services Center (GES DISC) [data set], https://doi.org/10.5067/VWSABTO7ZII4, 2019.

OCO-2/OCO-3 Science Team, Payne V., Chatterjee A.: OCO-2 Level 2 geolocated XCO2 retrievals results, physical model, Retrospective Processing V11r, Greenbelt, MD, USA, Goddard Earth Sciences Data and Information Services Center

690   (GES DISC) [data set], https://doi.org/10.5067/8Z3QQKHC4R4C, 2020.

Pan, S., Yang, J., Tian, H., Shi, H., Chang, J., Ciais, P., Francois, L., Frieler, K., Fu, B., Hickler, T., Ito, A., Nishina, K., Ostberg, S., Reyer, C. P., Schaphoff, S., Steinkamp, J., and Zhao, F.: Climate Extreme Versus Carbon Extreme: Responses of Terrestrial Carbon Fluxes to Temperature and Precipitation, J. Geophys. Res. Biogeosci., 125, doi:10.1029/2019JG005252, 2020.

695   Peters, W., Jacobson, A. R., Sweeney, C., Andrews, A. E., Conway, T. J., Masarie, K., Miller, J. B., Bruhwiler, L. M. P., Pétron, G., Hirsch, A. I., Worthy, D. E. J., van der Werf, G. R., Randerson, J. T., Wennberg, P. O., Krol, M. C., and Tans, P. P.: An atmospheric perspective on North American carbon dioxide exchange: CarbonTracker, Proc. Natl. Acad. Sci. USA, 104, 18925–18930, doi:10.1073/pnas.0708986104, 2007.

Piao, S., Wang, X., Wang, K., Li, X., Bastos, A., Canadell, J. G., Ciais, P., Friedlingstein, P., and Sitch, S.: Interannual

700   variation of terrestrial carbon cycle: Issues and perspectives, Glob Change Biol, 26, 300–318, doi:10.1111/gcb.14884, 2020.

Poulter, B., Ciais, P., Hodson, E., Lischke, H., Maignan, F., Plummer, S., and Zimmermann, N. E.: Plant functional type mapping for earth system models, Geosci. Model Dev., 4, 993–1010, doi:10.5194/gmd-4-993-2011, 2011.

Poulter, B., Frank, D., Ciais, P., Myneni, R. B., Andela, N., Bi, J., Broquet, G., Canadell, J. G., Chevallier, F., Liu, Y. Y.,

705   Running, S. W., Sitch, S., and van der Werf, G. R.: Contribution of semi-arid ecosystems to interannual variability of the global carbon cycle, Nature, 509, 600–603, doi:10.1038/nature13376, 2014.

Ramo, R., Roteta, E., Bistinas, I., van Wees, D., Bastarrika, A., Chuvieco, E., and van der Werf, G. R.: African burned area and fire carbon emissions are strongly impacted by small fires undetected by coarse resolution satellite data, Proceedings of the National Academy of Sciences of the United States of America, 118, doi:10.1073/pnas.2011160118, 2021.

710   Randerson, J. T., Thompson, M. V., Malmstrom, C. M., Field, C. B., and Fung, I. Y.: Substrate limitations for heterotrophs: Implications for models that estimate the seasonal cycle of atmospheric CO 2, Global Biogeochem. Cycles, 10, 585–602, doi:10.1029/96GB01981, 1996.

Reick, C. H., Gayler, V., Goll, D., Hagemann, S., Heidkamp, M., Nabel, Julia E. M. S., Raddatz, T., Roeckner, E., Schnur, R., and Wilkenskjeld, S.: JSBACH 3 - The land component of the MPI Earth System Model: documentation of version

715   3.2, Reports on Earth System Science, n/a-n/a, doi:10.17617/2.3279802, 2021.

Sellar, A. A., Jones, C. G., Mulcahy, J. P., Tang, Y., Yool, A., Wiltshire, A., O'connor, F. M., Stringer, M., Hill, R., Palmieri, J., and others: UKESM1: Description and evaluation of the UK Earth System Model, J. Adv. Model. Earth Syst., 11, 4513–4558, 2019.

Shi, Y., Matsunaga, T., Saito, M., Yamaguchi, Y., and Chen, X.: Comparison of global inventories of CO_2 emissions from

720   biomass burning during 2002-2011 derived from multiple satellite products, Environmental pollution (Barking, Essex 1987), 206, 479–487, doi:10.1016/j.envpol.2015.08.009, 2015.

Steiner, A. L.: Role of the Terrestrial Biosphere in Atmospheric Chemistry and Climate, Accounts of chemical research, 53, 1260–1268, doi:10.1021/acs.accounts.0c00116, 2020.

725 Taylor, T. E., O'Dell, C. W., Crisp, D., Kuze, A., Lindqvist, H., Wennberg, P. O., Chatterjee, A., Gunson, M., Eldering, A., Fisher, B., Kiel, M., Nelson, R. R., Merrelli, A., Osterman, G., Chevallier, F., Palmer, P. I., Feng, L., Deutscher, N. M., Dubey, M. K., Feist, D. G., García, O. E., Griffith, D. W. T., Hase, F., Iraci, L. T., Kivi, R., Liu, C., Mazière, M. de, Morino, I., Notholt, J., Oh, Y.-S., Ohyama, H., Pollard, D. F., Rettinger, M., Schneider, M., Roehl, C. M., Sha, M. K., Shiomi, K., Strong, K., Sussmann, R., Té, Y., Velazco, V. A., Vrekoussis, M., Warneke, T., and Wunch, D.: An 11-year record of XCO$_2$ estimates derived from GOSAT measurements using the NASA ACOS version 9 retrieval algorithm,
730 Earth Syst. Sci. Data, 14, 325–360, doi:10.5194/essd-14-325-2022, 2022.

Tian, H., Chen, G., Lu, C., Xu, X., Hayes, D. J., Ren, W., Pan, S., Huntzinger, D. N., and Wofsy, S. C.: North American terrestrial CO2 uptake largely offset by CH4 and N2O emissions: toward a full accounting of the greenhouse gas budget, Climatic change, 129, 413–426, doi:10.1007/s10584-014-1072-9, 2015.

Tramontana, G., Jung, M., Schwalm, C. R., Ichii, K., Camps-Valls, G., Ráduly, B., Reichstein, M., Arain, M. A., Cescatti,
735 A., Kiely, G., Merbold, L., Serrano-Ortiz, P., Sickert, S., Wolf, S., and Papale, D.: Predicting carbon dioxide and energy fluxes across global FLUXNET sites with regression algorithms, Biogeosciences, 13, 4291–4313, doi:10.5194/bg-13-4291-2016, 2016.

Valentini, R., Arneth, A., Bombelli, A., Castaldi, S., Cazzolla Gatti, R., Chevallier, F., Ciais, P., Grieco, E., Hartmann, J., Henry, M., Houghton, R. A., Jung, M., Kutsch, W. L., Malhi, Y., Mayorga, E., Merbold, L., Murray-Tortarolo, G.,
740 Papale, D., Peylin, P., Poulter, B., Raymond, P. A., Santini, M., Sitch, S., Vaglio Laurin, G., van der Werf, G. R., Williams, C. A., and Scholes, R. J.: A full greenhouse gases budget of Africa: synthesis, uncertainties, and vulnerabilities, Biogeosciences, 11, 381–407, doi:10.5194/bg-11-381-2014, 2014.

van der Werf, G. R., Randerson, J. T., Giglio, L., van Leeuwen, T. T., Chen, Y., Rogers, B. M., Mu, M., van Marle, M. J. E., Morton, D. C., COLLATZ, G. J., Yokelson, R. J., and Kasibhatla, P. S.: Global fire emissions estimates during 1997–
745 2016, Earth Syst. Sci. Data, 9, 697–720, doi:10.5194/essd-9-697-2017, 2017.

van Marle, M. J. E., Kloster, S., Magi, B. I., Marlon, J. R., Daniau, A.-L., Field, R. D., Arneth, A., Forrest, M., Hantson, S., Kehrwald, N. M., Knorr, W., Lasslop, G., Li, F., Mangeon, S., Yue, C., Kaiser, J. W., and van der Werf, G. R.: Historic global biomass burning emissions for CMIP6 (BB4CMIP) based on merging satellite observations with proxies and fire models (1750–2015), Geosci. Model Dev., 10, 3329–3357, doi:10.5194/gmd-10-3329-2017, 2017.

750 Vuichard, N., Messina, P., Luyssaert, S., Guenet, B., Zaehle, S., Ghattas, J., Bastrikov, V., and Peylin, P.: Accounting for carbon and nitrogen interactions in the global terrestrial ecosystem model ORCHIDEE (trunk version, rev 4999): multi-scale evaluation of gross primary production, Geosci. Model Dev., 12, 4751–4779, doi:10.5194/gmd-12-4751-2019, 2019.

Walker, A. P., Quaife, T., van Bodegom, P. M., Kauwe, M. G. de, Keenan, T. F., Joiner, J., Lomas, M. R., MacBean, N., Xu,
755 C., Yang, X., and Woodward, F. I.: The impact of alternative trait-scaling hypotheses for the maximum photosynthetic

carboxylation rate (Vcmax) on global gross primary production, The New phytologist, 215, 1370–1386, doi:10.1111/nph.14623, 2017.

Weber, U., Jung, M., Reichstein, M., Beer, C., Braakhekke, M. C., Lehsten, V., Ghent, D., Kaduk, J., Viovy, N., Ciais, P., Gobron, N., and Rödenbeck, C.: The interannual variability of Africa's ecosystem productivity: a multi-model analysis,
760   Biogeosciences, 6, 285–295, doi:10.5194/bg-6-285-2009, 2009.

Weir, B., Ott, L. E., Collatz, G. J., Kawa, S. R., Poulter, B., Chatterjee, A., Oda, T., and Pawson, S.: Bias-correcting carbon fluxes derived from land-surface satellite data for retrospective and near-real-time assimilation systems, Atmos. Chem. Phys., 21, 9609–9628, doi:10.5194/acp-21-9609-2021, 2021.

Wiedinmyer, C., Akagi, S. K., Yokelson, R. J., Emmons, L. K., Al-Saadi, J. A., Orlando, J. J., and Soja, A. J.: The Fire
765   INventory from NCAR (FINN) – a high resolution global model to estimate the emissions from open burning, Geosci. Model Dev., 4, 625–641, doi:10.5194/gmdd-3-2439-2010, 2011.

Williams, C. A., Hanan, N. P., Baker, I., COLLATZ, G. J., Berry, J., and Denning, A. S.: Interannual variability of photosynthesis across Africa and its attribution, J. Geophys. Res., 113, doi:10.1029/2008JG000718, 2008.

Williams, C. A., Hanan, N. P., Neff, J. C., Scholes, R. J., Berry, J. A., Denning, A. S., and Baker, D. F.: Africa and the
770   global carbon cycle, Carbon balance and management, 2, 3, doi:10.1186/1750-0680-2-3, 2007.

Wunch, D., Toon, G. C., Blavier, J.-F. L., Washenfelder, R. A., Notholt, J., Connor, B. J., Griffith, D. W. T., Sherlock, V., and Wennberg, P. O.: The Total Carbon Column Observing Network, Phil. Trans. R. Soc. A., 369, 2087–2112, doi:10.1098/rsta.2010.0240, 2011.

Yuan, W., Liu, D., Dong, W., Liu, S., Zhou, G., Yu, G., Zhao, T., Feng, J., Ma, Z., Chen, J., Chen, Y., Chen, S., Han, S.,
775   Huang, J., Li, L., Liu, H., Liu, S., Ma, M., Wang, Y., Xia, J., Xu, W., Zhang, Q., Zhao, X., and Zhao, L.: Multiyear precipitation reduction strongly decreases carbon uptake over northern China, J. Geophys. Res. Biogeosci., 119, 881–896, doi:10.1002/2014JG002608, 2014.

Yue, X. and Unger, N.: The Yale Interactive terrestrial Biosphere model version 1.0: description, evaluation and implementation into NASA GISS ModelE2, Geosci. Model Dev., 8, 2399–2417, doi:10.5194/gmd-8-2399-2015, 2015.

780   Zaehle, S., Friend, A. D., Friedlingstein, P., Dentener, F., Peylin, P., and Schulz, M.: Carbon and nitrogen cycle dynamics in the O-CN land surface model: 2. Role of the nitrogen cycle in the historical terrestrial carbon balance, Global Biogeochem. Cycles, 24, n/a-n/a, doi:10.1029/2009GB003522, 2010.

Zeng, N., Mariotti, A., and Wetzel, P.: Terrestrial mechanisms of interannual CO 2 variability, Global Biogeochem. Cycles, 19, doi:10.1029/2004gb002273, 2005.

785   Zhang, X., Wang, Y.-P., Peng, S., Rayner, P. J., Ciais, P., Silver, J. D., Piao, S., Zhu, Z., Lu, X., and Zheng, X.: Dominant regions and drivers of the variability of the global land carbon sink across timescales, Global Change Biology, 24, 3954–3968, doi:10.1111/gcb.14275, 2018.